

Practical Application of Wide Bandwidth Floating Emissive Probes and Wavelet Analysis to the X2 Nested Hall Thruster

IEPC-2013-352

*Presented at the 33rd International Electric Propulsion Conference,
Washington D.C., USA
October 6-10, 2013*

Michael S. McDonald*, Raymond Liang, and Alec D. Gallimore[†]
*Plasmadynamics and Electric Propulsion Laboratory (PEPL)
University of Michigan, Ann Arbor, MI USA 48109*

Floating emissive probe plasma potential maps of the X2 dual nested channel Hall thruster across a triad of operating conditions (inner, outer, and dual channel) at 150 V discharge voltage are presented. The maps extend from the thruster exit plane and thruster centerline to 3.5 mean outer channel radii (OCR) axially and 2.8 OCR radially. Together with measured floating potential maps, electron temperatures and temperature-corrected plasma potentials are also estimated over a slightly smaller domain, about 1.5 OCR axially by 1.5 OCR radially. Construction techniques for a compact quad emissive probe array with aspect ratio >100 are presented to address emissive probe mortality, and the design and characterization of a high bandwidth probe heating and measurement circuit with linear probe frequency response up to 100 kHz and sensitivity up to 1 MHz are given. These techniques are discussed in detail. Time-resolved fluctuation measurements show raw plasma potential oscillations (uncorrected for electron temperature) with RMS values from 10-30 V in the very near field over both discharge channels. These fluctuations largely die down within 0.5 OCR of the exit plane. The high bandwidth plasma potential measurements are used together with wavelet analysis to detect plasma potential oscillation spectra in the near field of the outer X2 discharge channel that match those corresponding to the breathing and rotating spoke modes detected by high speed imaging. The spoke oscillation spectral peaks are stronger in the very near field than the breathing mode peak, though downstream the breathing mode oscillation is dominant. Finally, a simple finite element model for emissive probe temperature as a function of heating current is included to assist in experiment design.

I. Introduction

The nested Hall thruster (NHT) is a promising concept for highly efficient packing of multiple high-power Hall thrusters into a compact footprint. The technology is especially attractive for thruster power levels above around 50 kW, where single-channel Hall thrusters become unwieldy for handling and fabrication. As part of a study of NHT stability and coupling effects,¹ and to improve our understanding of how the complex magnetic field structure of the NHT affects the overall plasma behavior, emissive probe maps were undertaken to generate high bandwidth, large area plume maps of the X2 across a “triad” of operating conditions consisting of similar operating points across single- and dual-channel operation.

Section 2 of this paper discusses experimental equipment and methods, with Section 3 focusing in great detail on the construction, circuit design and frequency response testing of the emissive probes. Section 4 discusses the application of wavelet analysis to rapidly injected plasma probes, explains why this tool offers significant advantages over Fourier analysis for short residence time data acquisitions, and illustrates the generation of periodograms from a wavelet transform similar to the traditional Fourier power spectrum. Section 5 presents the time-averaged plume maps of raw plasma potential directly from the probes, as well as estimates of electron temperature generated from the scaled difference of hot and cold emissive probe measurements and estimates of the true plasma potential, corrected for electron temperature. It also illustrates the detection of large amplitude plasma potential oscillations in the very

*Karles Postdoctoral Fellow, Naval Center for Space Technology, Naval Research Laboratory, Washington D.C. This work was performed while a postdoctoral researcher at the University of Michigan. msmcdon@umich.edu.

[†]Arthur F. Thurnau Professor, Department of Aerospace Engineering, Director of the Plasmadynamics and Electric Propulsion Laboratory.

near field over the exit plane on channel centerline at the frequencies corresponding to rotating spoke propagation, as confirmed by high speed video. Section 6 summarizes these key results. Finally, an appendix is included developing a simple finite element model for required emissive probe heating currents, intended for sizing required power supplies in experiment design and observing likely sensitivities of filament temperature to heating current. The short MATLAB code implementing the model for the probes used in this work is also included.

II. Experimental Setup and Methods

A. Vacuum Facility

All experiments were conducted in the Large Vacuum Test Facility (LVTF) in the Plasmadynamics and Electric Propulsion Laboratory (PEPL) at the University of Michigan. The LVTF is a stainless steel-clad vacuum chamber 9 m long and 6 m in diameter, with an approximate volume of 200 m³. It is brought to rough vacuum by two 2000 CFM blowers backed by four 400 CFM mechanical pumps. Seven CVI TM-1200 re-entrant cryopumps with LN₂ baffles and a nominal pumping speed of 500,000 L/s on air or 240,000 L/s on xenon achieve high vacuum base pressure in the low 10⁻⁷ to high 10⁻⁸ Torr range. During the 150 V X2 triad testing, operating pressures were 6.3 × 10⁻⁶ Torr, 1.6 × 10⁻⁵ Torr and 2.2 × 10⁻⁵ Torr for inner, outer, and dual channel operation respectively.

B. Nested Hall Thruster

The X2 is a 10-kW class laboratory model dual-channel nested Hall thruster (NHT) developed at the University of Michigan Plasmadynamics and Electric Propulsion Laboratory under support from the Michigan / AFRL Center of Excellence in Electric Propulsion (MACEEP).² The X2 was intended as a technology demonstrator or proof-of-concept to investigate the operational characteristics of NHTs. Multiple channels optimized for different power ranges give the X2 and NHTs in general an extremely wide power throttling range, which can be spanned at high efficiency by selectively sharing operation between channels. The dual-channel configuration provides for three different types of operation at constant power in a single package: high thrust-to-power operation at high current and low voltage in dual-channel operation, high- I_{sp} operation at high voltage and low current on the smaller inner channel, and a compromise medium I_{sp} capability in outer channel operation.³ Liang noted, referring to work by Jacobson⁴ and Spores⁵, that “[a]vailable literature predating the X2 shows mostly conceptual consideration for NHTs with only a single mention of a development effort.”⁶ Busek also developed an approximately 6-kW dual channel Hall thruster in the mid-2000s under a SBIR contract.

Both X2 channels share a centrally mounted lanthanum hexaboride cathode, similar to the one used on the H6 Hall thruster,⁷ and for these tests are powered from separate power supplies with a shared cathode common. Joint operation of both channels from a single power supply is also possible. The X2 discharge channels are identical in width, length and anode cross-section with a similar magnetic field shape. The thruster body is electrically grounded to the chamber while the anode and cathode float relative to ground with a fixed discharge voltage applied between them. A RC discharge filter consisting of a 220 μF capacitor rated to 800 VDC placed between each anode and the cathode common together with the resistive load of the thruster discharge itself is used to protect the main discharge power supplies and reduce voltage ripple at the thruster during current oscillations.

The three 150 V operating conditions presented here are known as a “triad”. An X2 NHT operating triad consists of three operating conditions: both individual channel operating cases (inner and outer) and the joint dual-channel case. Within a triad other discharge parameters are held constant, including discharge voltage, discharge current density or mass flow density in each channel, and magnetic field settings. In particular both sets of magnets for the inner and outer channels are kept engaged, even when only one channel is operating. The only differences across a triad are which channels receive anode flow and have discharge voltage applied, and the total cathode mass flow rate since a fixed cathode flow fraction relative to total anode flow is maintained. As a result of the fixed cathode flow fraction, the cathode floating potential moves from closest to furthest from ground as the total mass flow rates decrease from dual to outer to inner channel operation.¹

1. Prior work on the X2

Work to date on the X2 has primarily been aimed at constant-power performance measurements on a thrust stand,³ supported by time-averaged plume diagnostics necessary for decomposition of performance efficiency into physically

meaningful sub-efficiencies relating to mass utilization, voltage utilization, and others as part of a standard Hall thruster efficiency architecture.^{6,8,9} In these prior works Liang also presents a brief discharge current oscillation study noting that at several dual-channel operating conditions the channels share a breathing mode frequency, and in other cases noting that the breathing mode frequency of one channel appears in the power spectrum of the opposite channel. Of particular note, those cases with shared frequency behavior between channels exhibited the largest amplitude current oscillations, ranging from 10-70% of the mean discharge current. More recently, a study of triads at 150 V and 250 V by McDonald focused on inter-channel coupling by searching for differences in plasma oscillations between single- and dual-channel operating modes.¹ That work found only minor changes in discharge current oscillation amplitudes and frequencies moving from single- to dual-channel operation, with partial coupling of the larger outer channel's discharge current oscillations into the inner channel at the 150 V condition.

C. Motion Stages

Two perpendicular motion stages, one radial and one axial, were used to generate 2D maps of plasma properties. The radial stage is a 1.5 m long Aerotech ATS62150 ball screw stage driven by a stepper motor. It is used in open loop position feedback mode with a 15 V string potentiometer to move the Hall thruster in the radial direction during data acquisition. The axial stage is a 0.5 m long Parker Trilogy T2S I-Force Ironless Motor Positioner, a linear motor capable of a maximum of 6 g acceleration and 5 m/s velocity. This stage is better known as the High-speed Axial Reciprocating Probe (HARP), and is used for axial injection of plasma probes into the thruster plume. It operates in a closed loop position feedback mode with 5 μm resolution Renishaw LM10 encoder. Both stages are operated by Aerotech motion controllers, an Aerotech MP10 for the radial stage and an Aerotech CP20 for the axial HARP stage, that are in turn automated from LabView. A leveling table underneath the thruster permits vertical alignment of emissive probe filaments to thruster centerline to within ± 0.5 mm.

The Aerotech CP20 controller uses pulse-width modulation (PWM) speed control. PWM is a duty-cycled square wave current, and the sharp corners of the square wave with large dI/dt cause ringing in nearby circuits. Since the PWM frequency is 20 kHz, in the middle of the frequency range of interest for Hall thrusters, the PWM electrical interference requires careful attention to grounding techniques for time-resolved measurements. Running the three phases of current driving the HARP separately through grounded coaxial cable from the CP20 controller to the linear motor and use of an additional Aerotech Motor Filter Module (MFM) on the CP20 output significantly reduced the inductive noise. Nevertheless, it was necessary to remove the emissive probe signal cables from the HARP enclosure and cable track to eliminate the noise completely. This required a portion of the probe cabling to be exposed directly to the thruster beam during testing, so that section was doubly protected by grounded stainless steel sleeving overlaid with fiberglass tape.

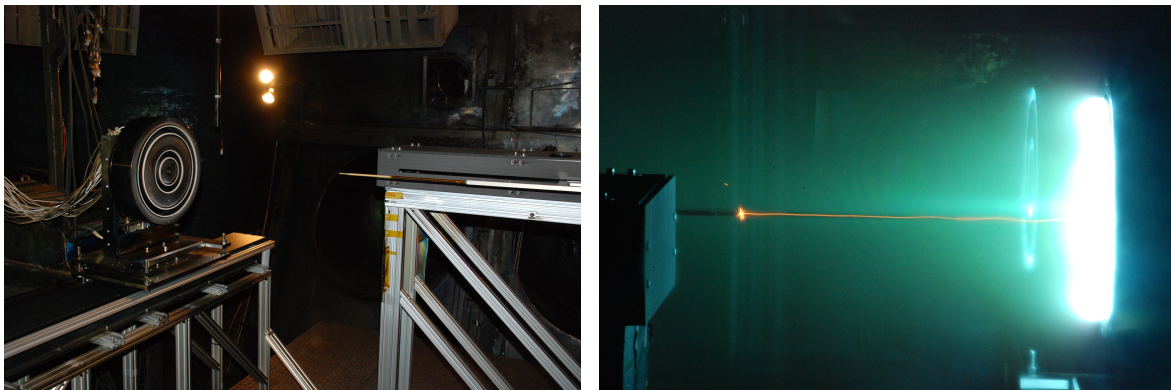


Figure 1. Left, Motion stage setup showing X2 on 1.5 m radial ballscrew stage and quad emissive probe array on HARP; Right, Long-exposure photo of probe injection showing some wobble

During mapping the HARP is injected approximately 500 mm in 500 msec. This injection speed balances reduced residence time in the near field (minimizing plasma perturbation and probe ablation) with probe arm vibration under rapid acceleration (compromising position fidelity). A typical HARP probe trajectory is shown in Figure 11, with a peak velocity in the middle of the move of 1.5 m/s. The probe spends more time near the limits of the shot since the HARP accelerates and decelerates in these regions. A time-lapsed photo of a hot emissive probe injection in Figure 1

shows the slight vibration of the probe at this speed.

The vibration visible in Figure 1 is due to the radial extent of the probe rake, designed to keep the body of the HARP enclosure outside of the line of sight of the X2 outer channel. The radial uncertainty is about ± 2 mm, judging from the photo and high-speed imaging of several shots. Since the shots are highly repeatable, relative radial position at the same axial location between shots is not affected. Later Langmuir probe diagnostics described by Sekerak used an improved rake design and stabilizing bridge built by Liang to significantly reduce this vibration. The bridge was so named due to its similarity with the cue bridge in pool and billiards, and was positioned near the probe tip when in the home position.

D. Floating Emissive Probe

1. Principles of Operation

Floating emissive probes heat a low work-function material to thermionic emission in a plasma. The hot filament emits electrons until it floats nearly to the local plasma potential, when electrons begin to reflect back to the filament and prevent the potential from rising further. The exact difference between the hot probe floating potential (henceforth the “raw” or “uncorrected” plasma potential) and the true plasma potential is between $1-2 T_e$, with recent Hall thruster experiments suggesting $2 T_e$ is the best estimate.¹⁰

Emissive probes are exceedingly fragile, prone to an early, fiery death, and typically tested to destruction (see Figure 2). The extreme thermionic emission temperatures promote evaporative mass loss from the hot filament. A runaway scenario develops as the mass loss reduces the filament diameter, increasing the filament resistance and thus Ohmic power deposition for the same heating current. The temperature rises further, the rate of evaporative mass loss accelerates and eventually the filament burns up. This is compounded in Hall thruster investigations by constant high-energy ion bombardment and, for near-field and internal measurements, the harsh Hall current which can rapidly ablate tungsten filaments and alumina probe bodies.¹¹



Figure 2. Evaporative mass loss leads to emissive probe failure. Left, a virgin filament mounted in a dual-bore alumina tube. Middle, a filament intact after testing but showing preferential mass loss at the hottest region, the tip. Right, a filament destroyed during testing. In the moment of failure the temperature runs away leading to globules of melted tungsten at each end.

2. Design Summary

The challenges of Hall thruster plume mapping with emissive probes, the effort that went into overcoming them, and the sincere hope of saving others from some small part of that effort motivated an extensive discussion in Section III of the design considerations, construction techniques and lessons learned during probe design. This section provides a concise summary of the probe design more suitable for those not interested in building their own probes.

The emissive probes consist of a 0.1 mm diameter 0.6% thoriated tungsten filament bent into a hairpin loop of 1 mm diameter. The loops is secured by crimping into very small copper tubes inserted into a dual bore alumina tube. Four such filament assemblies are mounted into a larger quad bore alumina tube and the resulting quad probe array is crimped into a longer stainless steel tube, which is secured into an aluminum probe rake mounted to the HARP body. The total length of the probe, from stainless steel tube base to filament tip, is approximately 1 m with diameter < 1 cm, for an aspect ratio of >100 .

The emissive probe outbound and return current lines run through coaxial cable from the vacuum chamber flange approximately 5 m away. Current is supplied by a Kepco ATE 25-4M 100W power supply in current control mode remotely controlled by a 0-5 V analog control voltage passed through an isolation amplifier. The control voltage ramps

the heating current from a warm-idle level keeping the filament red hot when not in use to a full emission current just before probe injection.

E. High-speed camera

High speed video was taken using a Photron SA5 FASTCAM with a Nikon ED AF Nikkor 80-200mm lens at its maximum aperture $f/2.8$. Videos with 256x256 pixel resolution at 87,500 fps were acquired after equilibrating at each triad operating condition, in most cases with the probes and HARP structure moved to approximately half a meter off thruster centerline to avoid perturbation of the plasma. Occasional videos taken during probe injections showed little if any change in oscillation frequencies as long as the probe did not penetrate the discharge channel exit plane, which was true for all data presented here.

A more detailed discussion of the high speed camera diagnostic for rotating spoke analysis is given in a companion paper,¹² as well as in previous publications.¹³⁻¹⁵

III. Emissive Probe Design and Construction

This section gives a more detailed overview of the design, construction, and lessons learned from emissive probing in the near-field of high-power Hall thrusters. It is primarily intended for experimentalists planning to use emissive probes, high speed stages, or both for near-field and/or internal Hall thruster interrogation. Others should feel free to skim or skip this section. Special attention is given to high speed measurements and probe characterization to achieve 100s kHz to MHz frequency response.

A. Overview

Plume mapping with emissive probes in the very near-field of the thruster presents a conflicting set of requirements:

1. A long reach, to keep the motion stage far downstream of the thruster and minimize plasma perturbation
2. Low cross-sectional area, to minimize thruster perturbation when the probe enters the dense near-field plasma
3. Quick insertion and retraction, to prevent filament and probe ablation in the harsh near-field plume
4. Stiffness to bending, to minimize vibration amplitude during rapid probe insertion and removal
5. Redundancy by virtue of multiple probes, as probes will still burn out eventually
6. Relative affordability, again since probes will still burn out eventually

The first two requirements drive a high aspect ratio (length/diameter) probe assembly, in this case using a telescoping design to achieve a total length >1 m while minimizing tip cross section to ~ 5 mm. The third requirement dictates the use of a high speed axially reciprocating motion stage (the HARP, Section C). The stiffness requirement is responsible for the telescoping design, use of a rigid probe rake, and reduction of peak HARP velocity to strike a balance between low vibration and short probe residence time at peak extension. The final two requirements motivated the use of commercial off-the-shelf parts to construct multiple probes in a single body. The final design used a quad array of 4 filaments on a single probe arm <1 cm in peak diameter and >1 meter long, for an aspect ratio > 100 .

B. Probe Physical Construction

1. Filament

We used 0.6% thoriaed tungsten wire 0.1 mm (0.004") in diameter in the form of hairpin loops with a 1 mm (.040") loop diameter. Previous Hall thruster near-field investigations have often used .127 mm (.005") diameter wire,^{11,16-20} with some use of .15 mm (.006")²¹ and .05 mm (.002").¹⁰ Occasionally larger diameter wires are used for more robust probes in low-gradient plasma regions far downstream where spatial resolution is less important than lifetime, for example .5 mm (.020") wire by Jameson.²²

Tiny imperfections in the hairpin loop can fatally compromise an emissive probe, as the slightly higher local resistance at kinks or constrictions increase heating and accelerate necking and failure. We found a simple method

to make a very smooth loop is to use a drill bit of the desired loop diameter as a mandrel, clamping each end of the filament between thumb and forefinger and pulling it tightly around the bit. A 5-8 cm long filament is enough to grasp, form and install into copper tubing. Music (or piano) wire cutters were used to cut the hard tungsten filaments, since they notch and ruin unhardened cutting surfaces and will often splinter as well.

The choice of filament diameter is a balance of mechanical assembly, electrical heating, filament survivability and space-charge concerns. The filament is often a loop connected to lead wires in an insulating body such as an alumina tube. The diameter must be small enough to fit in the alumina tube and bend to an appropriate loop diameter. Probe tip heating must also balance input power with radiative and conductive cooling. Larger wires require a larger heating current and overall power to reach thermionic emission, affecting the choice of power supply, but they will survive better as evaporative and sputtering mass losses cause a proportionally smaller reduction in filament area.

In the limit of a long wire, neglecting conduction effects, a balance between Ohmic heating power, thermal radiation cooling and thermionic electron emission cooling estimates the required current to achieve a given temperature:

$$I = \left(\frac{2\pi r^3}{\rho} \left(\sigma \epsilon T^4 + \Phi_W A_G T^2 \exp\left(\frac{-q\Phi_W}{k_B T}\right) \right) \right) \quad (1)$$

where r is the filament radius, ρ is the resistivity, ϵ is the emissivity and σ is the Stefan-Boltzmann constant. This equation tends to be accurate for length/diameter ratios above about 20 and says that, for a given temperature, heating current goes $I \propto r^{3/2}$. A more detailed finite element thermal model including conduction effects for estimating required heating currents and temperature profiles is given in the appendix.

Emissive probes in Hall thrusters are generally made of tungsten (W) wire, often with the addition of 0.6 - 2% thoria (ThO). Thoria was first added to reduce grain growth in tungsten filaments at high temperature,^{23,24} but it was found to dramatically reduce the work function Φ_W from 4.5 V to about 2.6 V.²⁵ The work function figures prominently in the Richardson-Dushman equation for thermionic emission current density,

$$j = A_G T^2 \exp\left(\frac{-q\Phi_W}{k_B T}\right) \quad (2)$$

$$A_G \equiv \lambda_R A_0 = \lambda_R \frac{4\pi m_e k_B^2 q}{h^3} \quad (3)$$

where A_G is the material-specific general Richardson-Dushman constant, defined as the product of a material-specific factor $\lambda_R \in (0, 1)$ and the universal Richardson-Dushman constant $A_0 = 120 \text{ A/cm}^2\text{-K}^2$.²⁶ Depending on the source, either A_G or λ_R may be found in the literature. For pure tungsten, $A_{G,W} = 60.2$ and for thoriated tungsten $A_{G,W/ThO} = 3$.^{24,27}

Thermionic emission current density curves as a function of temperature are shown in Figure 3, and the emission current densities at 2000 C are compared to the electron saturation current densities at various plasma densities and temperatures. Given an expected range of $T_e = 3 - 30 \text{ eV}$ and $n_e = 10^{16} - 10^{19} \text{ cm}^{-3}$, a pure tungsten filament would have to operate well in excess of 2000 C to reach saturated emission for thruster plume mapping. Thoriated tungsten drastically increases the emission current at a given temperature, enabling reduced temperatures to reach equivalent emission levels and increasing filament lifetime.

If possible, filament carburization (heating in a hydrocarbon atmosphere) reduces evaporation rates and extends filament lifetime by about 50%.²⁴ Carburizing forms a surface layer of very hard tungsten carbide, so it is best performed after the filament has been bent to the desired shape. However, in practice it is difficult to find capable commercial vendors interested in carburizing small batches of filaments for research.

It is also becoming harder to find thoriated tungsten suppliers. While it has been used for emissive probes since 1914²⁸ and was widely used in welding electrodes for decades, thorium is radioactive with decay by low-energy alpha particle emission. The material is safe in routine use for the experimentalist – the alpha particles have insufficient energy to penetrate the skin, even using bare hands – but it is dangerous to internal tissues if inhaled or ingested. As a result, health hazards from fine thoria dust inhalation in production facilities have gradually phased the material out of the welding industry in favor of ceriated and lanthanated tungsten. While welding rods are widely available in these other materials, wire is not. The only reliable commercial supplier of small wire quantities for research we are aware of is Goodfellow Corporation.

A final plasma-related concern mentioned by some investigators²⁰ is that probe thermionic emission not form an appreciable fraction of the discharge current of the device under test, motivating a smaller probe in some cases. However, while this concern is valid for Langmuir probes in electron saturation drawing current from the plasma,

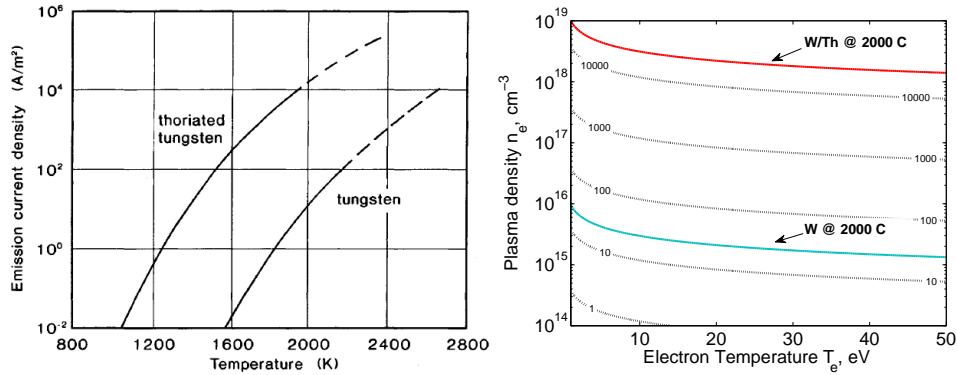


Figure 3. Left, Emission current densities for pure and thoriated tungsten.²⁵ Right, electron saturation currents as functions of plasma density and electron temperature, overlaid with thermionic emission curves at 2000 C.

it is not generally for emissive probes since in full space-charge saturation they mostly balance the incoming flux of electrons with those that are thermionically emitted. A more appropriate concern regarding plasma perturbation would be the different electron temperature between the incoming and emitted electron populations, but this effect has not been experimentally addressed.

2. Probe Body

The 100X aspect ratio probe body is built from four Omega TRX-164-116 1.6 mm x 0.4 mm x 30 cm (1/16" x 1/64" x 12") alumina dual-bore tubes potted into an Omega FRX-11614 6.4 mm x 1.6 mm x 30 cm (1/4" x 1/16" x 12") alumina quad-bore tube chopped to 25 cm to allow the smaller tubes to project slightly forward of the larger tube body. All tube dimensions are given as (OD x ID x *l*). Each smaller alumina tube held its own emissive filament of a 0.1mm diameter (.004") thoriated tungsten (XX%) curled into a 1 mm hairpin loop (.040") and fed into tiny copper tubes (see next section) crimped using needlenose pliers to make secure electrical contact. The axial distance from filament loop tip to copper junction was 2.5 mm.

The small alumina tubes with their filaments were secured into the larger tube with Aremco Ceramabond 571. Dabbing the outside of the smaller tube with adhesive before sliding it inside the larger tube and wiping away the excess secures the probe in place with minimal visible adhesive. Initially, when visible ceramabond was left exposed on the probe, an orange plasma glow appeared when placed in the thruster ion beam. This minimal exposure technique reduced the presumed ablation or outgassing of the ceramabond significantly. Ceramabond was also used as a "potting" substance to isolate the electrical leads exiting the alumina tube.

After baking to cure the ceramic adhesive, the ~30 cm long alumina assembly with lead wires was partially inserted into a 7.9 mm x 6.4 mm x 56 cm precision ground stainless steel tube (McMaster P/N XXXX) and secured using a tube cutter to circularly crimp the stainless tube onto the alumina tube underneath in two to three places for good concentricity. The total length matched the axial range of the HARP to reach the exit plane at peak extension, while the diameter was sized by available quad-bore alumina tubing. The probe arm secures into a welded aluminum probe rake by set screws (Figure 7, top left) which is bolted in turn to the HARP. The set screws are lock-wired to prevent loosening under the vibration of repeated HARP shots.

We used alumina (Al₂O₃) for the insulating probe body for its low cost, good mechanical and dielectric strength and high melting temperature (1950 C). Other options include mullite (Al₆Si₂O₁₃), which has a slightly lower melting temperature (1600 C) but has also been used.²¹ Beryllia, diamond, and silicon nitride are generally not suitable.²⁰ In some cases where low secondary electron emission or high thermal conductivity are needed, boron nitride is used as a cap, collar or coating over an alumina base. For example, in the Hall thruster discharge channel high current densities and electron temperatures can fracture an alumina tube due to thermal shock unless boron nitride is used as a heat spreader.^{2,10,20} This work focused on near-field investigations of the X2 only, so did not use BN collars or coatings. In later internal investigations of the X2 with floating emissive probes, Liang used both BN collars and BN coatings using a water-based paint.

Beware the tolerances on the many small parts required to fit together in such a telescoping assembly. For example, a 0.38 mm tube may range from 0.35-0.40 mm, so a filament will not always fit in a tube of matched size, and likewise

a small alumina tube will not always fit in a larger one. In practice we bought several extra of each component, and usually around half would fit together into a probe (“winning the tolerance lottery”) and half would find their way to other uses in the lab.



Figure 4. Example of a 0.1 mm diameter (.004”) emissive probe filament with crimped copper tubes for lead wires. From left, a filament used for plume mapping with 2.5 mm exposed filament from tip to copper junction; middle, a filament shown in extreme closeup with a human hair overlaid for scale (this filament not used for testing); right, a CAD cutaway showing the filament with copper tube leads in a 1.6 mm OD dual-bore alumina tube.

3. Electrical Connections

As noted above, each filament in the quad array is mounted into copper tubing as electrical lead wires. Very fine copper tubing with good tolerance is widely produced for the electrical discharge machining (EDM) industry, and we used 0.4 mm x 0.127 mm x 30 cm (.015” x .005” x 12”) copper tubes purchased from Saturn Industries for less than \$1 USD per tube. The filament attaches to the tube by sliding inside the tube inner diameter, where it is gently crimped by needlenose pliers. Once the filament is secure, the copper tubes slide down the dual-bore alumina tubes. Pin-and-socket connections join the copper tubing extending from the rear of the alumina tubes to 16 AWG magnet wire sufficiently long to reach down the stainless steel tube. All four filaments were installed into the alumina assembly, had sockets crimped on, and were potted and air-dried for 1 hour before curing at 93 C (200 F) for 1-4 hours.

The pin-and-socket connections to the magnet wire were sealed with Kapton polyamide tape, and then the stainless tube was crimped in place over the larger quad-bore alumina tube. Heat shrinking was too bulky to fit inside the stainless tube. Before crimping the stainless tube in place, the continuity of each filament was double (triple!) checked and isolation between filaments and from filament to the stainless tube was confirmed. The exposed magnet wires at the end of the stainless tube were connected, again by pins and sockets, to the center conductors of about 1 m of coaxial cable terminated in SMA connectors. These connections were heatshrinked to secure the pins and sockets and as strain relief to prevent the weight of the cables from pulling the filament connections loose.

The coaxial cable section was exposed to the thruster ion beam while dangling from the HARP probe rake for the duration of the experiments (often several hours), and so was doubly shielded, first by a grounded stainless steel sleeve and second by a double wrapping of fiberglass tape. The fiberglass suffered, but the cables survived well and were re-used between test runs. The SMA connectors were adapted to BNC and run through a further ~5 m coaxial cable to the chamber exit, carefully routed out of the line of sight of the thruster ion beam. The coaxial cable shields were individually grounded at the vacuum chamber flange.

In general, the filament must connect to lead wires from the vacuum chamber feedthrough all the way to the plasma area of interest, sometimes several meters. The leads make the filament section as short as practical, since the resistance of tungsten increases by an order of magnitude from room temperature to 2000 °C and the voltage drop across filament and leads is a source of measurement error (see Section ??). Short filaments and low-resistance lead wires (large diameter and/or high conductivity) also enable lower-wattage heater power supplies.

Since probes are often tested to destruction, affordable lead wire materials are desirable. Examples of lead wire materials include nickel,²⁹ tantalum,^{19,21} molybdenum, and copper.^{16,17,20} For alumina bodies, narrow boreholes and high operating temperatures make securing the leads to the filament challenging. Bore diameters limit lead wire diameter and often preclude mechanical fastening techniques such as butt splicing or pin and socket connections, while the temperatures prohibit soldering. Remaining options include spot-welding,^{19,29} frictional fits between the lead wire and a lengthy hairpin filament with additional small-diameter tungsten wires to wedge the filament in tightly,^{10,11,17,20}

optionally with the use of a ceramic or quartz adhesive to cap the bore, or crimp attachments from the filament to small copper tubes serving as leads.³⁰

Spot-welding to metals such as nickel, tantalum or molybdenum is acceptable if the probe geometry does not create too large a voltage drop or excessive Ohmic heating on the leads, but copper is not suitable for spot-welding. Gold-coated nickel wire has been used with good effect, as it is both spot-weldable due to the nickel core and solder-able due to the gold coating. Another material that is both solder- and spot weld-compatible is Monel, an alloy of nickel and copper. The friction fit technique is effective but tedious, though a jeweler's loupe and a pair of fine tweezers help enormously. However, this technique is not always reproducible – the same number of additional wires may not pack into every alumina tube, and over-forcing them risks accidentally bending the hairpin loop and starting over, so it is difficult to know when a filament is secure. Haas' use of a quartz adhesive cap to seal the bore and hold the lead wires in place is also delicate and sometime challenging work. Threading tungsten wire into a small copper tube and crimping is simpler, but care must be taken to expose a sufficiently long filament for the temperature to drop from emitting temperatures of 2000+ °C to below copper's melting point at 1085 °C.

Melting is especially a problem for probes rapidly injected into a plasma, where melted copper can wick to the probe tip, eject onto the filament during deceleration, or loosen the frictional fit and allow the filament to escape in part or in full (see Figure 5). Hargus, upon discovering that ejected copper may also deposit on other experimental apparatus (described as a “particularly eventful failure”), promptly switched to tantalum.²¹ The finite element model in the appendix does not predict the required filament tip-to-copper distance correctly, primarily because it neglects thermal contact resistance at the junction. Instead, the 2.5 mm axial distance from filament tip to copper junction in this work was experimentally verified for the 0.1 mm diameter filament and 0.4 mm copper tube. No melting or copper ejecta were observed with this filament arrangement during the X2 mapping.

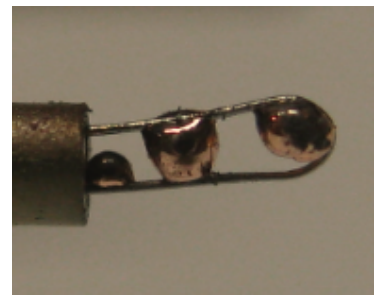


Figure 5. Potential failure mode of an emissive probe using copper lead wires to the filament with additional tungsten wires for a frictional fit. The copper was placed too close to the tip and melted during probe heating. Molten copper globules were ejected during HARP insertion and retraction.

C. Heating and Measurement Circuit

The emissive probe circuit heats the filament to thermionic emission and measures its floating potential, which is approximately the plasma potential. Complicating factors include measuring tip potential from a remote location outside the vacuum chamber, while the probe is floating at tens to hundreds of volts, and while the filament is heated to the edge of saturated emission but no further.

Probe tip potential is measured using the circuit in Figure 6. The measurement point is a tap between two matched series resistors placed in parallel with the filament resistance, measured with respect to ground. For ideal, perfectly matched lead lines and resistors negligible fuse resistance, the filament tip voltage is equal to the resistor tap voltage. Practically, the tap potential is calibrated to the filament potential by measuring both values simultaneously at atmosphere while sourcing small test currents of a few hundred milliamperes through the circuit. The resistors are large relative to the filament ($R = 50 \Omega$) so minimal current flows through them during probe operation, but small enough to avoid inadvertently low-pass filtering the probe signal (Section 3.5). The sacrificial fast-blow fuse protects the resistors when a filament fails and the power supply attempts to force the commanded current across the resistors instead. Setting the voltage limit on the power supply may also be sufficient to avoid resistor burnout, depending on the voltage and resistance.

While not shown in the circuit, the total probe voltage drop was monitored with a multimeter as a passive diagnostic of filament health – as the filament degraded the same heating current produced higher voltage drops due to increased resistance from the thinning filament tip. However, this technique was too imprecise to actively reduce filament current as it degraded to prolong filament life. The total probe resistance, leads and filament included, was about 1.5 Ω cold but increased during heating for a drop of 5-7 V at 2-3 A heating current.

For the delicate filaments used here and the dozens of emissive probe firings per map the heating profile is automated using LabView software to reduce human error. LabView directs a Measurement Computing USB-3103 analog output voltage controller to generate a 0-5 V control signal, which passes through an Analog Devices AD210 isolation amplifier with unity gain to a programmable Kepco ATE 24-5M DC power supply in remote current control mode. The smooth, repeatable ramp reduces thermal shock, the USB 3103 16-bit digital-to-analog voltage control provides milliamper-level heating current resolution, and the automation (mostly) eliminates human error while the AD210

maintains probe isolation from ground. The Kepco power supply is also powered through an isolation transformer to float properly.

Each probe is constantly supplied with a “warm-idle” current, chosen as the threshold where the probe begins to glow red. The heating current ramps from warm-idle to a hot emitting current over 10-20 seconds, pauses at full current for 2-3 seconds before the HARP fires, and immediately ramps down to warm-idle after firing. The HARP firing is also controlled from LabView. For these probes the warm-idle current varied between 1.5-2.5 A due to variations in probe construction, with the emitting current generally 0.3-0.5 A higher. At full emission the probe is very bright white, though emission is always judged based on the measured probe voltage, not color (Section 3.6). The heating schedule and warm-idle current level were not optimized; so faster ramp times or higher warm-idle currents might provide similar filament life.

Several factors motivate keeping the probe at a warm idle when not actively taking a measurement. Long durations at emitting temperature promote evaporative mass loss, but filament failure from thermal shock in hot-cold cycling is a real risk for small filaments. At least once during testing an intact filament was allowed to cool completely when testing concluded for the day, with careful ramping from warm-idle to cold over 120 seconds. The next day, the filament was no longer intact, presumably broken under thermal stress along recrystallized grain boundaries. Afterward once a filament was heated for the first time we maintained a warm idle between measurements and tested until probe failure, never cooling the filament. A warm idle also keeps the probe body closer to thermal equilibrium, making it easier to hone in on the heating power that produces saturation without overshooting during the slight delay between applying a heating current and the probe temperature response.

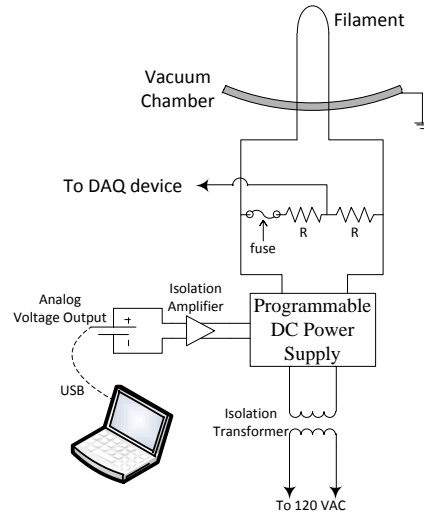


Figure 6. Emissive Probe Measurement Circuit

D. Data Acquisition Hardware

After the circuit in Figure 6 averages the probe lead voltages, the signal is passed to an Agilent DSO-3024X 4-channel oscilloscope. Since the oscilloscope full scale is only 40 V, for interrogation of the near field over the two discharge channels where the potential approaches the 150 V discharge voltage the signal also passes through a 10:1 Avex Electronics 600-10-2 compensated oscilloscope probe. Each acquisition is sampled at 2 MHz for 500 ms, sufficient to capture the entire probe insertion and part of the retraction.

The Agilent oscilloscope is capable of sampling at 4 GHz with 8-bit resolution over its user-selected full scale. However, the memory capacity of the oscilloscope is only 10^6 points per channel. The scope fills this buffer completely, so a 1 s acquisition is at 1 MHz, 500 ms is at 2 MHz, and so on. In normal acquisition for a 1 s acquisition the scope samples at 4 GHz, but only one point each microsecond is recorded and the rest are thrown out to achieve the 1 MHz rate. We use the built-in high-resolution acquisition mode instead, where each recorded point is generated by averaging all 4 GHz points acquired in the corresponding window. This reduces the measurement error by a factor of $N^{1/2}$, where N is the number of averaged samples. For the 2 MHz, 500 ms acquisitions used here, 2000 4 GHz readings are averaged per recorded datapoint. This increases the normally 8-bit digital resolution of the scope by $\log_4(N) = 5.5$ bits to over 13-bit resolution, or about 10 mV on a 100 V full scale. This increase in resolution comes at the cost of effectively low-pass filtering the signal in the MHz range.

Common data acquisition hardware choices are either an oscilloscope or a dedicated data acquisition (DAQ) device or card. Oscilloscopes provide higher bandwidth than DAQs, often GHz-level instead of kHz-MHz, at the cost of fewer digital bits of resolution, usually 8 or at most 12 bits for an oscilloscope compared to 16-bit for most DAQs. High-resolution scope acquisition modes can sacrifice the higher bandwidth to recover some of the loss in bit depth. Oscilloscopes typically accept larger input voltage ranges than DAQs, reducing the need to pass the signal through additional isolation amplifiers or other complicated circuitry which can deteriorate frequency response. However, DAQ devices are often simpler to integrate into automated experiments, for example using LabView software, and can continuously acquire data at peak frequency while scopes have limited memory buffers. The choice depends heavily

on the individual experiment needs, but even when planning to use a dedicated DAQ, an oscilloscope is simpler and safer to start with for checking voltage ranges, noise levels and other initial troubleshooting.

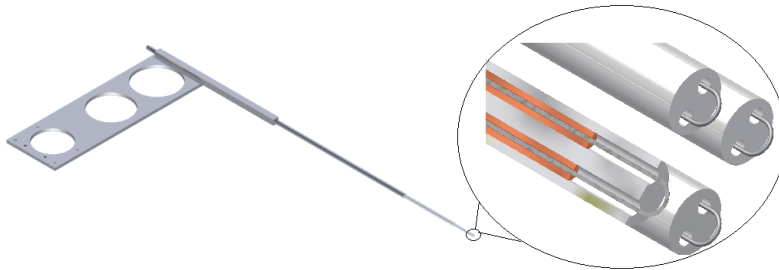


Figure 7. CAD Model of emissive probe construction showing probe mounted in probe rake with closeup of quad array probe tip

E. Probe Frequency Response

For time-resolved measurements of plasma potential oscillations, probe frequency response up to 100 kHz was desired, sufficient to resolve the Hall thruster breathing and spoke modes in the low single to few tens of kilohertz at well past the Nyquist frequency. Probe circuit frequency response was characterized using a broadband “chirp” signal, a modulated sine wave swept from 10 Hz to 1 MHz over 10 ms periods for 500 msec duration. A function generator inside the vacuum chamber applied the chirp signal directly to the filament tip via a length of bare copper wire delicately hanging from the thoriated tungsten loop. This signal passed through the circuit of Figure 6 as discussed before to an oscilloscope, both with and without the 10:1 compensated voltage divider. The signal was also teed off at the function generator and passed directly through to the oscilloscope as quickly as possible via 6 m of coaxial cable.

The synchronous record of both signals acquired at 2 MHz was Fourier transformed and used to generate a Bode plot of the gain and phase delay as a function of frequency for the circuit. An example Bode plot for a 10X voltage division is shown in Figure 8, with no phase lag and near unity gain (after accounting for the 10X division) up to 100 kHz with resonances near 120 kHz and 800 kHz before falling off slightly approaching 1 MHz. The transfer function computed for the Bode plot can even be used to construct a custom filter to account for these resonances, but since they are small and outside the frequency range of interest this was not done for the data presented here.

Compensated oscilloscope probes were selected for voltage division over the combination of resistive voltage dividers and isolation amplifiers used previously by Reid, Linnell and Shastry for their higher bandwidth and much lower noise levels than the AD210 and AD215 isolation amplifiers. The compensated oscilloscope probes, also known as passive or attenuation probes, combine a resistive and capacitive voltage divider with a tunable capacitance such that, by matching the tunable capacitance on the probe to that of the DAQ or oscilloscope, they can provide constant voltage division regardless of frequency up to the probe bandwidth.^{31,32} The 10X probe was compensated properly for the Agilent oscilloscope by tuning until it accurately reproduced the sharp corners and flat top of a 1-kHz square wave.

1. Initial Poor Results and Low-Pass Filtering

While the final design had good response up to 100 kHz and acceptable sensitivity up to 1 MHz, initial efforts yielded much poorer frequency response and suggest that the resistances used in the voltage averaging circuit apparently can combine with the stray capacitance in the circuit to form an effective low-pass RC filter. The main source of stray capacitance was the power supply internal capacitance used to maintain voltage control under changing loads. Initially using ~ 10 kΩ resistors in the circuit of Figure 6 combined with the internal power supply capacitance ~ 1 mF produced a probe response attenuated by half (i.e., a 3-dB cutoff) by the 10-30 kHz range.

Since the emissive probes ran in current control on a static load, this internal capacitance was unnecessary. The Kepco ATE-series power supplies have an optional “fast mode” bypassing most of the internal capacitance, reducing the total about 1000X from ~1 mF to ~1 μF. Together with reducing the resistance R from 10 kΩ to 50 Ω, probe bandwidth recovered as seen in Figure 8. Still, while the simple RC filter cutoff frequency is $f_c = 1/(2\pi RC)$, the observed behavior did not follow this formula closely. This formula would give a cutoff frequency of only 12 kHz for the configuration used in this experiment, which experimentally appeared to have a cutoff frequency near 1 MHz. To take another example, the circuit used by Reid in Figure 9 successfully detected nearly 20 kHz plasma potential

oscillations (see Figure 7 in that paper).²⁰ The circuit used a $\sim 10\text{ M}\Omega$ resistor, which even assuming a very low 10 pF stray capacitance would still give a calculated cutoff frequency of $< 2\text{ kHz}$, so apparently a RC filter model alone is insufficient to predict circuit frequency response.

Short of modeling the entire circuit behavior in a circuit simulator such as SPICE, best practice for high frequency measurements with this circuit configuration appears to be to minimize the resistance R and circuit stray capacitance, and to verify probe response experimentally by applying a known waveform to the probe tip to ensure accurate signal reproduction. As a lower bound, sizing the resistance R to be about 50 times the hot filament resistance ensures that only about 1% of the heating current passes through the resistors while avoiding low-pass filter effects.

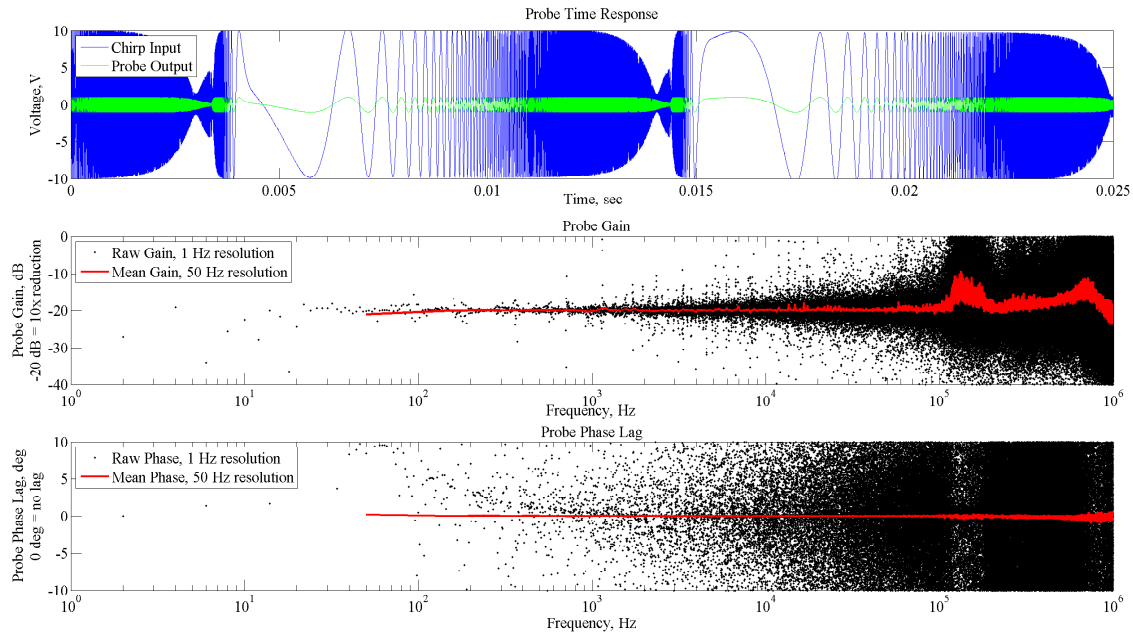


Figure 8. Bode plot showing emissive probe frequency response to a chirp signal. Top, a 10 Hz - 1 MHz chirp is measured directly from the probe tip (blue) and through a 10:1 compensated oscilloscope probe (green.). Middle and bottom, Bode gain and phase plots show the transfer function between the input and output signals. The raw Bode data (black) is quite noisy, but a simple windowed average (red) shows flat phase and relatively flat gain to near 100 kHz. Two small resonances appear between 100 kHz and 1 MHz, which are also visible in the time-domain plot at top as dips in amplitude in the solid blue regions.

F. Testing for Saturation

We found judging saturation of a floating emissive probe to be a frustrating and stressful process. Even with four probes on an array, only rarely did more than two produce useful data. Previous investigators Linnell, Jameson, Reid and Haas suggest gradually increasing the heating current until further increases produce no further increase in measured floating potential. Unfortunately, in practice this often culminates in too much heating and a burnt out filament.

To find the saturation current, rather than a single measurement at one point in the far field, the probes were injected on channel centerline to the exit plane, and the entire plasma potential profile was recorded. The heating current was incrementally raised on successive shots until no discernible difference in potential was visible with 25 mA additional heating current.

In retrospect, this saturation testing technique probably hastened the probes' demise. Later emissive probe investigation of the X2 found greater survivability of filaments by injecting them fully into the channel, such that residence in or near the Hall current was brief and the majority of residence time was spent in the quiet depths of the channel. This was especially true at higher discharge voltages, where higher electron temperatures and ion energies make a harsher near field environment. In these cases a boron nitride collar or painted coating on the probe body is necessary as a heat spreader and suppressor of secondary electron emission.

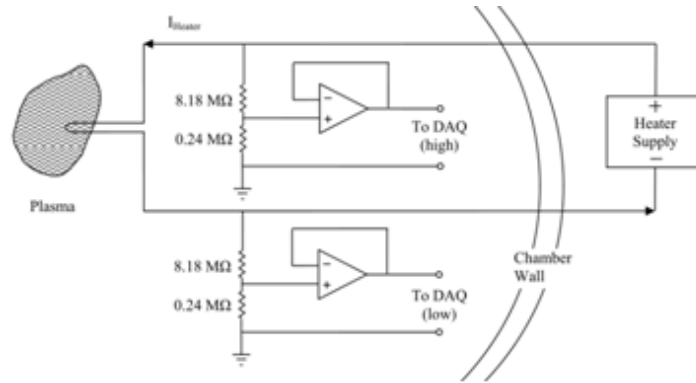


Figure 9. A circuit used by Reid for floating emissive probe voltage division and isolation using two DAQ channels. Despite the MΩ-level resistors, Reid was able to resolve a 20 kHz breathing mode with this circuit, which based on a simple model of RC low-pass filtering would seem improbable. This indicates that, while reducing R and C as much as practical to improve probe frequency response certainly helps frequency response, purely judging behavior from a $f_c = 1/2\pi RC$ cutoff model is too simplistic.

For future investigation, or were we to repeat these experiments, three stages of saturation testing are probably advisable. First, the thermal model in the Appendix should give estimates of required heating current for a given temperature accurate to within a few tenths of an amp, useful for choice of power supply. Next, a stationary Langmuir probe measuring plasma potential and electron temperature in the far field “home position” of the emissive probe would enable honing in on the saturation current in a safe region without the complication of additional heat flux from the Hall current. Finally, slightly greater electron emission and thus higher heating current is necessary for saturation in the higher density plasma of the very near field. With the far-field saturation current in hand, one would hope a relatively small number of injections fully into the channel could find the near-field saturation current, prolonging filament life.

Several authors note that thoriated tungsten requires a special conditioning process. The material is first heated to a temperature of about 2800 K to flash the thoria to pure thorium metal. After this initial flashing, the filament is “activated” by reducing the temperature to 1900-2200 K to allow a thorium monolayer to diffuse to the filament surface. After activation the temperature should be maintained <2100 K where the diffusion rate of thorium to the surface is sufficient to overcome the rate of thorium evaporation at the surface.^{23,24} Langmuir cites a flashing period of 3 minutes, while Harbaugh cites a 15-30 minute activation period. While we initially attempted this process, it was difficult to estimate the heating current for the “flashing” stage accurately, and evaporative mass loss was visibly apparent in the slowly increasing voltage drop across the filament during the flashing period. Instead, high energy (300 eV) argon ion sputtering has previously been demonstrated to activate a thoriated tungsten filament without flashing,³³ and the good results ultimately obtained with un-flashed thoriated tungsten filaments in this work indicates that the ~150 V xenon ions probably served the same purpose.

IV. Numerical Technique: Wavelet Analysis for Frequency Analysis with Temporal Resolution

Giving a brief preview of the experimental results in Section V, in the X2 near field substantial plasma oscillations occur (Figure 10). A relatively clear breathing mode is visible in the bottom plot, but the plasma potential seems to have several different oscillation frequencies present. By visual inspection the signal appears to display short-lived bursts of coherent oscillatory behavior of various frequencies over timescales on the order of half a millisecond. This seems qualitatively similar to brief coherent bursts of spoke propagation in high-speed video before the spokes tear apart and re-form, sometimes with different mode numbers.

Efforts to simulate the potential oscillations as white noise fail, as the extensive oscilloscope averaging in high-resolution mode mostly eliminates random noise. On the other hand, the usual tool to characterize oscillations in Hall thrusters is Fourier analysis, perhaps with an eye toward temporospatial data fusion of the type pioneered by Lobbia.³⁴ Fourier analysis does not work well when analyzing HARP injections due to poor time resolution of the discrete Fourier transform (DFT). There is no balance possible between temporal and frequency resolution in the DFT.

Section 4A first describes the challenge of Fourier analysis of a rapidly moving probe signal. It turns out that

what would be ideal would be a technique to resolve transient behavior at different frequencies with good temporal resolution, a hybrid between time-domain and frequency-domain analysis. This is the strength of wavelet analysis, described in Section 4B. Sections 4C-4D explain how to use the wavelet transform to generate a periodogram from the wavelet transform that is conceptually similar to the usual DFT.

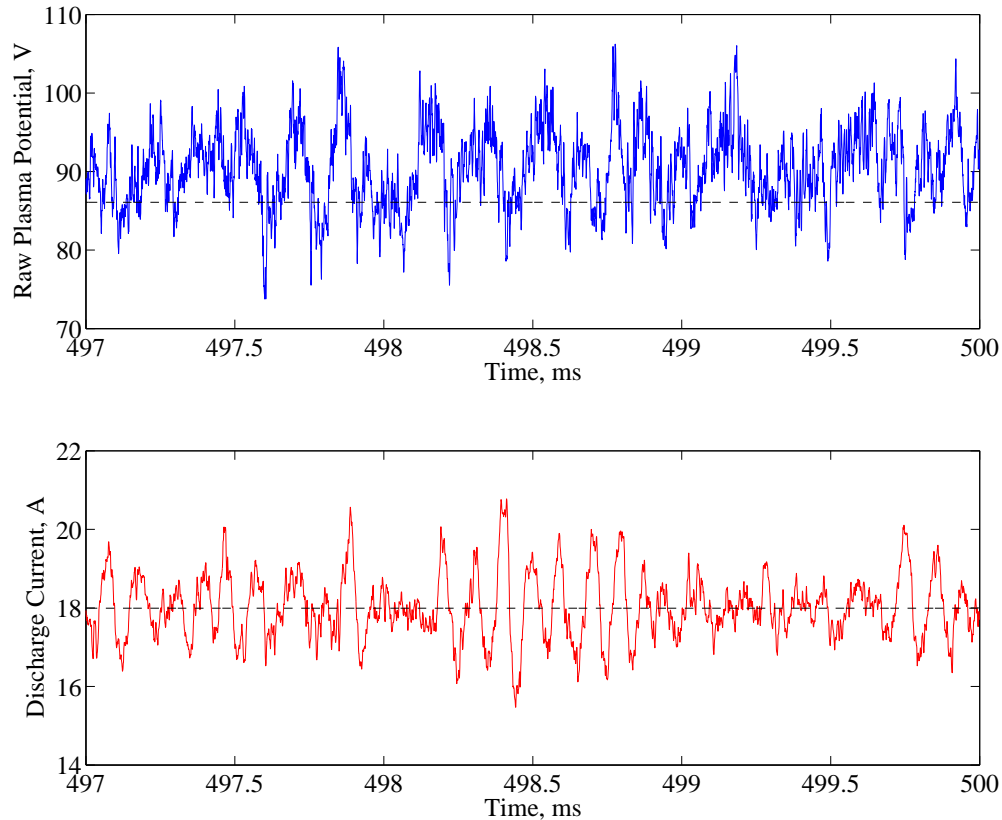


Figure 10. Plasma potential in the very near field ($z \approx 2$ mm) and discharge current of the X2 outer channel during HARP probe injection on outer channel centerline at 150 V operation.

A. Challenges of Fourier Analysis of a Moving Probe: Resolution and Noise

The Fourier spectrum of a discrete signal may be characterized by two frequencies, the Nyquist frequency f_N and the frequency resolution Δf . The Nyquist frequency is half the sampling frequency f_s and can be raised at will by ever faster sampling. The frequency resolution of the spectrum is the inverse of the sampling duration of the discrete signal, $\Delta f = 1/\Delta t$. For a moving probe, the sampling duration at a given spatial point is then determined by the probe residence time near that point. This resolution can be improved at will by moving the probe ever more slowly. Thus, the upper bound of f_N is limited by available DAQ systems, and the lower bound of Δf is limited by how long a probe resides in / can tolerate exposure to a region of the plasma.

For a typical HARP shot profile, the residence times Δt and corresponding frequency resolutions Δf are shown in Figure 11. For a 1 mm spatial resolution, the frequency resolution is quite poor in many regions of the plasma, on the order of 1 kHz. Ideally the resolution would be at least an order of magnitude better, on the order of 100 Hz. Only at the very limits of travel where the probe accelerates and decelerates is this possible. Considering that the region of most intense oscillation extends axially to $z=20$ mm, the figure shows DFTs of the plasma potential signal in the 20 mm closest to the exit plane as well as a DFT of the entire rest of the shot from $z=20$ mm to $z=510$ mm.

This, then, is why Fourier analysis is poorly suited for this type of data analysis. The example cited above for Fourier analysis³⁴ used a rapidly swept Langmuir probe with fixed position in the X2 far field sampled for 1 second

at several points in a 2D grid. Noise corrupts a DFT, so a common noise reduction technique is to take data for a long time, break the data into chunks, compute DFTs for each chunk and average them. The long duration of data acquisition in that case allowed large-scale averaging while maintaining good frequency resolution, and ultimately created excellent reconstructions of oscillatory behavior in the far field. Unfortunately, the rapid injection required for near-field interrogation to minimize plasma perturbation and probe ablation gives only a few to tens of milliseconds per centimeter of axial travel. The time spent on a single grid point by Lobbia is the time available for an entire injection here, making DFTs terribly noisy and coarse. An alternative would be to build up residence time over many shots, i.e., 100 shots with 10 ms residence time instead of 1 acquisition of a full second, but floating emissive probes are not made for such longevity. Another method is required: wavelets.

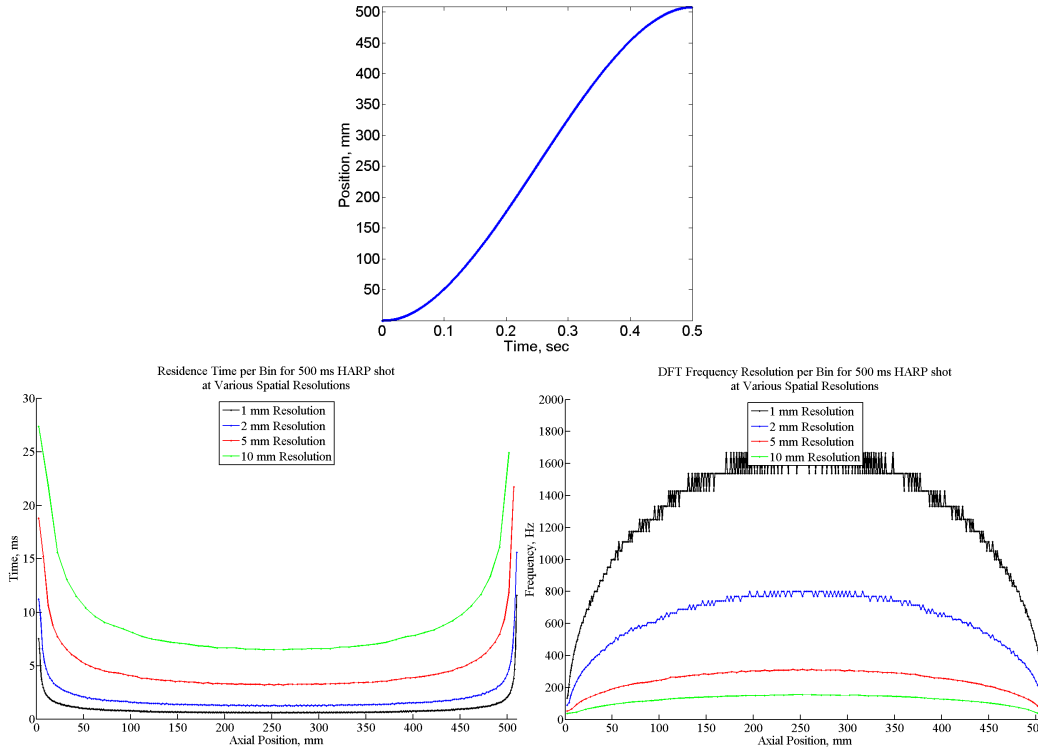


Figure 11. Left, Residence Times vs. Spatial Resolution, right, Achievable DFT Resolution vs. Spatial Resolution

B. How wavelets work

Fourier analysis of a signal is localized in frequency but not in time. For example, the DFT of a digital recording of an orchestral symphony might show peaks for every note played by every instrument in the performance, but the resulting jumble of peaks carries no information on note durations or harmonies – it would give the same results if the orchestra played the piece backwards, or if every performer chose the order in which to play their notes at random.

Wavelets form a complete set of basis functions localized in both frequency and time; for example, the common Morlet wavelet is a sinusoid modulated by a Gaussian. The sinusoid has a particular frequency, and the Gaussian has a particular shift in time, such that the resulting wavelet is a pulse of an approximate frequency (“scale”) and an approximate time. Due to the Heisenberg uncertainty principle wavelets sacrifice some precision in frequency to become localized in time (the technical term is “support”), with different wavelet functions such as the Morlet striking different balances between the two domains. Wavelets of various scales are convolved with the input signal, producing a correlation function. Large values indicate a resonance between the wavelet and the signal, thus identifying in time when a particular frequency associated with that scale is present. In a wavelet transform all possible scales of wavelets are convolved with the input signal (just as in the Fourier transform all frequencies are analyzed), producing a two-dimensional output similar to a spectrogram. In the orchestral analogy, a wavelet might be a pulse with frequency corresponding to middle C and a 16th note duration. Convolved with the recording, it would resonate every time

that tone was played. Repeatedly passing wavelets of various frequencies (i.e, C#, D, etc.) and durations (half note, quarter, eighth) through the recording would be sufficient to reconstruct the entire orchestral score, just as with the sines of various frequencies from the Fourier basis. However, the localization in time (compact support) turns out to be an advantage.

The detailed mathematics of wavelets are beyond the scope of this paper. They are explained very well by Torrence³⁵, who also provides MATLAB code for implementing wavelet transforms on 1D datasets.^a We use the Morlet wavelet in this paper because it is simple to describe, relatively well-known, and because the frequency with peak response to a given Morlet wavelet is very close to the apparent frequency from the generating sine wave. The code from Torrence is used with only minor modifications to allow GPU acceleration.

C. Comparison: Wavelet Transforms vs. Spectrograms

Fourier analysis is sometimes applied to a signal of long duration using the short-time Fourier transform (STFT) to produce a spectrogram. This technique breaks up a signal into a number of segments which are each Fourier analyzed separately. The DFTs of each segment are then stitched together into a surface plot, presenting a picture of how the DFT changes over time. Because DFT windowing sacrifices data near the edge of each segment, segments are often chosen to overlap by as much as 50%. This is called Welch's method. A baseline signal for comparison is the measurement of discharge current in the X2 during HARP interrogation of the plasma. The thruster is operating on the outer channel only, and the discharge channel is perturbed toward the end of the time series because the probe was not inserted fast enough. Figure 12 shows how spectrograms of the sample discharge current signal compare to a wavelet transform.

Two spectrograms are shown, one breaking the signal into 8 segments, the other into 50 segments. Because of the 50% overlap, 16 distinct columns appear in the 8-segment spectrogram and 100 columns appear in the 50-segment spectrogram. These images illustrate the weak temporal resolution of STFTs. The STFT best detects frequencies the inverse of the signal duration, i.e., the minimum frequency detectable (100 Hz for a 10 ms signal). Transient higher frequency information in the signal is smeared out.

Unlike the STFT the wavelet transform does not fix the number of segments; instead, wavelets are a class of multiresolution analysis technique with coarser resolution at low frequencies and progressively higher resolution at higher frequencies. This advantage over the STFT is apparent in the bottom of Figure 12, where the temporal resolution is ever finer at higher frequency.

D. Comparison: Wavelet vs. DFT Periodograms

The periodogram is a more familiar plot than the spectrogram. The periodogram is simply the power spectral density of a full signal, without any attempt at temporal resolution by signal chopping as in the STFT or multiscale analysis as in the wavelet transform. Nevertheless, wavelets still offer substantial advantages in smoothing the power spectral density. Periodograms are often smoothed by Welch's method by generating a spectrogram as in the previous section and then averaging over time; the same principle may be applied to a wavelet transform. This is shown in Figure 13.

The raw periodogram, equivalent to a spectrogram with one segment, has excellent frequency resolution and terrible noise artifacts. The progressive use of a larger number of segments reduces noise by sacrificing frequency resolution. The average over the wavelet transform is far smoother than any of the DFT periodograms because at each frequency it has been averaged over the maximum possible number of correlation values from the convolution of appropriately scaled wavelets with the full signal. The scale of the y-axis in the wavelet-generated periodograms is given in arbitrary units for the time being until further research can establish the exact scaling to present them in the usual units of $(\text{Amplitude})^2 / \text{Hz}$ for a DFT power spectral density.

The drawback to this technique is that some of the sharpness in the frequency peak that is apparent in the DFT periodograms is lost. This is a consequence of the uncertainty principle mentioned earlier: sine waves have an exact frequency, while wavelets have a slight spread in frequency since they are really pulses of finite duration. Different wavelet families have sharper frequency properties and may be more suitable to resolving sharper peaks, but no effort has been made to optimize the choice of wavelet. MATLAB offers a built-in wavelet toolbox as well, with many more wavelets, but the nested subroutines are nearly impossible to decipher, so eventual optimization of this technique would require further research and custom coding. Finally, note that the sinusoid basis of Fourier analysis is merely a

^aWavelet code in MATLAB, FORTRAN and IDL may be found at: <http://paos.colorado.edu/research/wavelets/software.html>

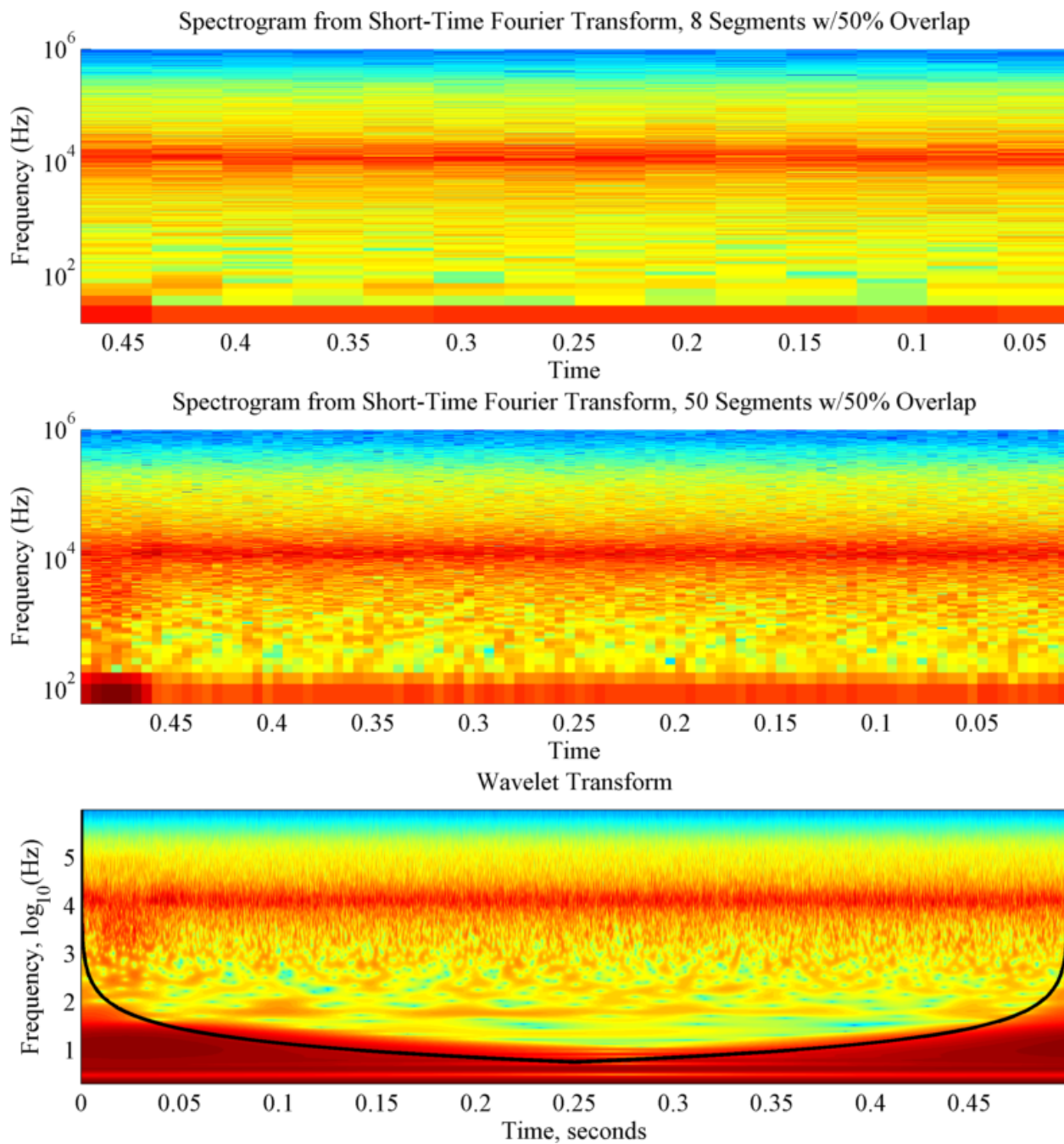


Figure 12. Comparison of STFT spectrograms with the wavelet transform of the X2 outer channel discharge current during a HARP injection. Top, a STFT spectrogram with 8 segments and 50% overlap; middle, a STFT spectrogram with 50 segments and 50% overlap, and bottom a wavelet transform of the same signal. The wavelet transform adapts to give higher time resolution at higher frequencies. Ignore the reversal of the time axis between the plots; all three plots in fact show the same time and the slightly elevated oscillations to the left side indicate plasma perturbation as the probe approached the exit plane.

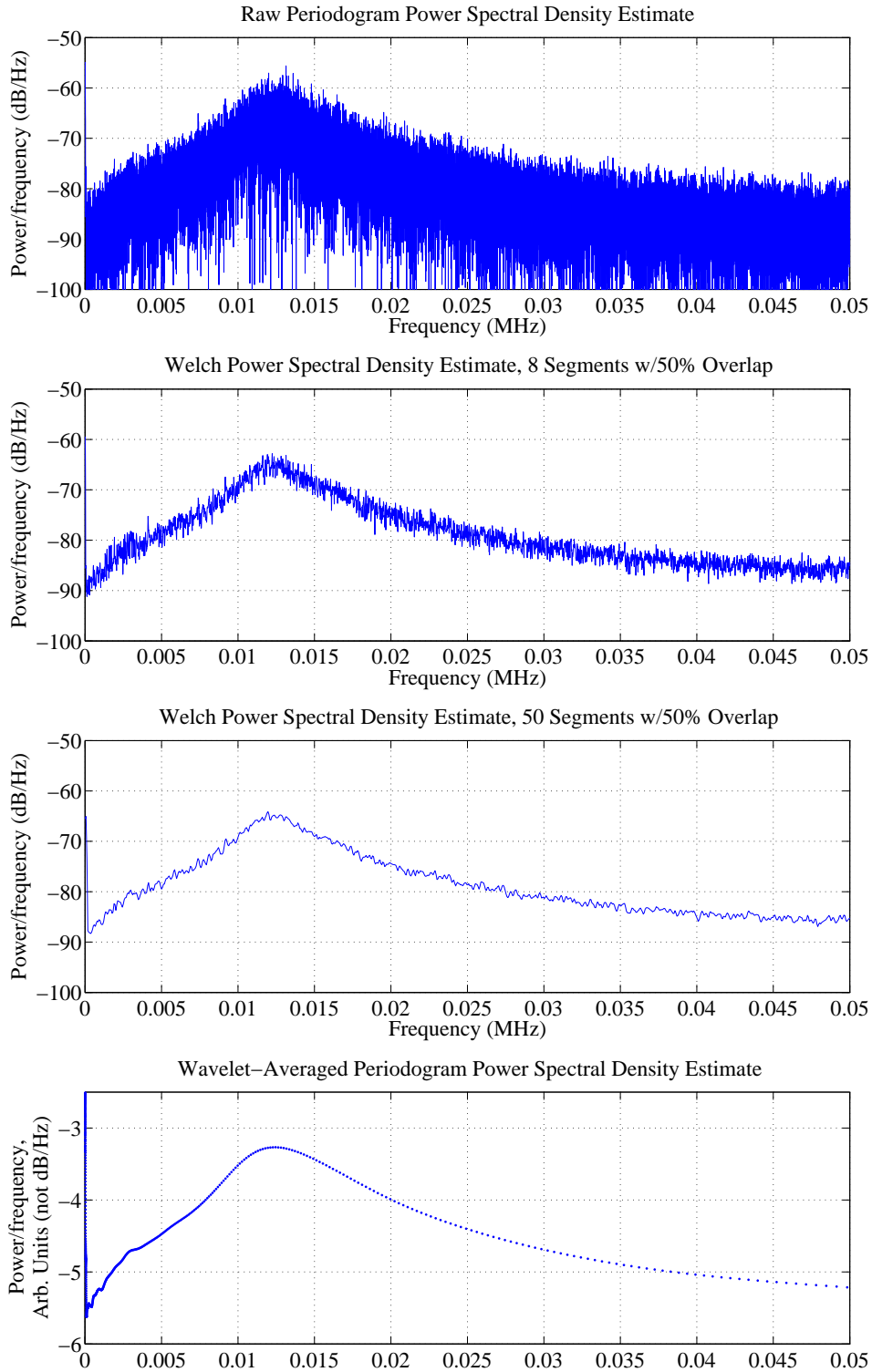


Figure 13. Comparison of periodograms derived from the discrete Fourier transform (DFT) vs the wavelet transform. The top three plots show DFT-generated periodograms with various levels of smoothing by using Welch's method of averaging over subintervals. This is mathematically identical to an average over time in the surface plots of the spectrograms in the previous section. The bottom plot shows a periodogram generated from averaging in time over the wavelet transform surface plot from the previous section. The smoothness is noticeably improved. The variable spacing of the points in the wavelet periodogram is because the scales in the wavelet transform were chosen logarithmically to save computation time.

wavelet at one extreme end of the spectrum – absolute frequency resolution with no temporal resolution at all.

V. Experimental Results

A. Estimate of T_e for V_p Correction

Using maps of floating potential together with the maps of emissive probe plasma potential, one can estimate the electron temperature and use it to correct the raw emissive probe plasma potential to further estimate the true plasma potential concealed by sheath effects over the probe. In a Maxwellian plasma, the floating potential is about 6 electron temperatures below the plasma potential:

$$V_p - V_f = T_e \ln \left(0.61 \sqrt{\frac{2\pi m_e}{M_i}} \right) = -5.78 T_e [eV]$$

Taking the raw plasma potential measured by the emissive probe as an underestimate of the true plasma potential by a factor of two electron temperatures based on recent measurements in Hall thrusters by Sheehan,¹⁰ an approximate electron temperature is computed from the difference between hot and cold emissive probe traces, as well the approximate corrected plasma potential. The error in the estimate of T_e using this method was estimated at 17% by Raitses.³⁶

B. Time-averaged maps: V_p and T_e

Time-averaged maps of the raw plasma potential from the emissive probes were generated from a full set of 30-40 axial injections. The 2 MHz acquisitions along each axial profile were binned into 1 mm segments and averaged, with >1000 points in each millimeter bin. The resulting axial strips of averaged data, which are radially separated by 2-10 mm, were interpolated using a piecewise cubic Hermite interpolating polynomial (MATLAB 'pchip') scheme in the radial dimension to produce 1 mm radial resolution as well. While the axial extent of acquisition was about half a meter, some of the low gradient downstream axial range is not shown in the figures below.

The time-averaged maps of raw (uncorrected) plasma potential, estimated electron temperature and estimated full corrected plasma potential are given in Figures 14-22.

1. Inner Channel

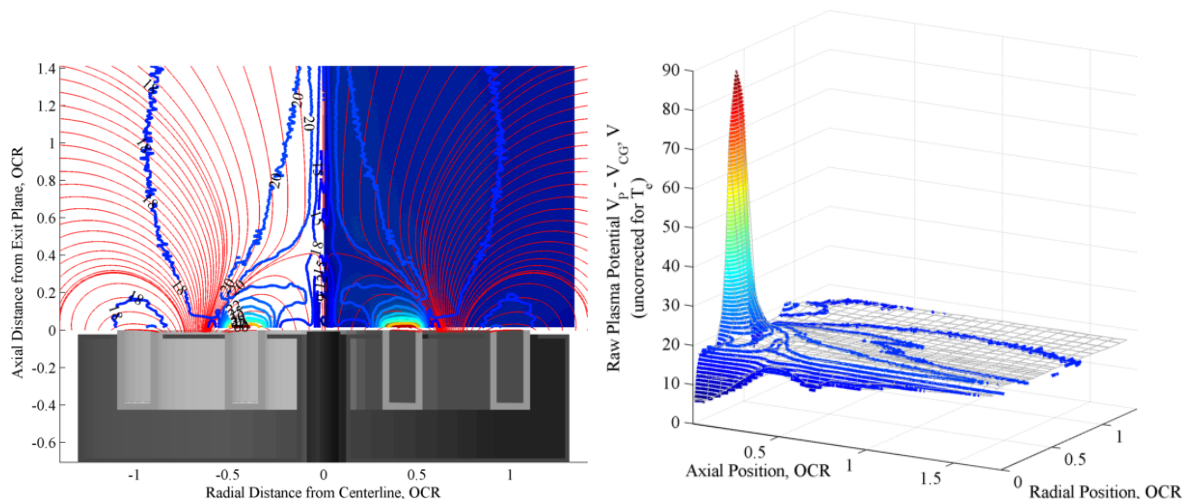


Figure 14. Raw Plasma Potential Measured from Emissive Probe, Uncorrected for T_e , Inner Channel Operation

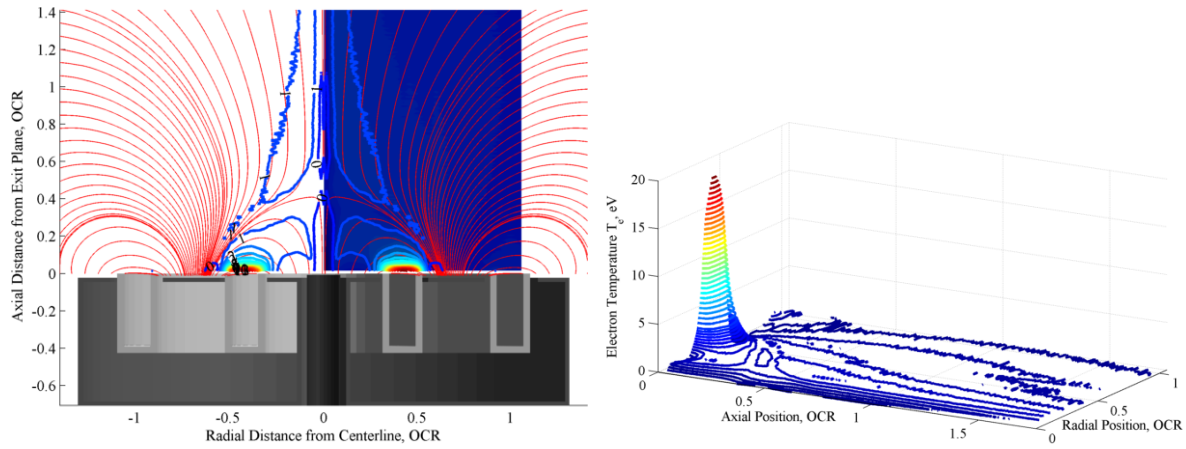


Figure 15. Estimated Electron Temperature T_e from Hot and Cold Emissive Probe Maps, Inner Channel Operation

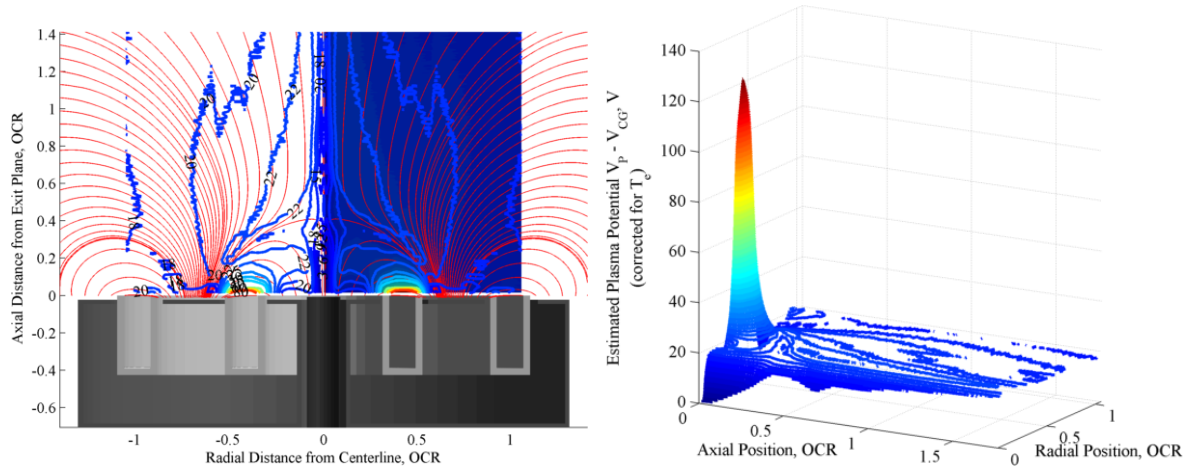


Figure 16. Estimated Plasma Potential Corrected for T_e , Inner Channel Operation

2. Outer Channel

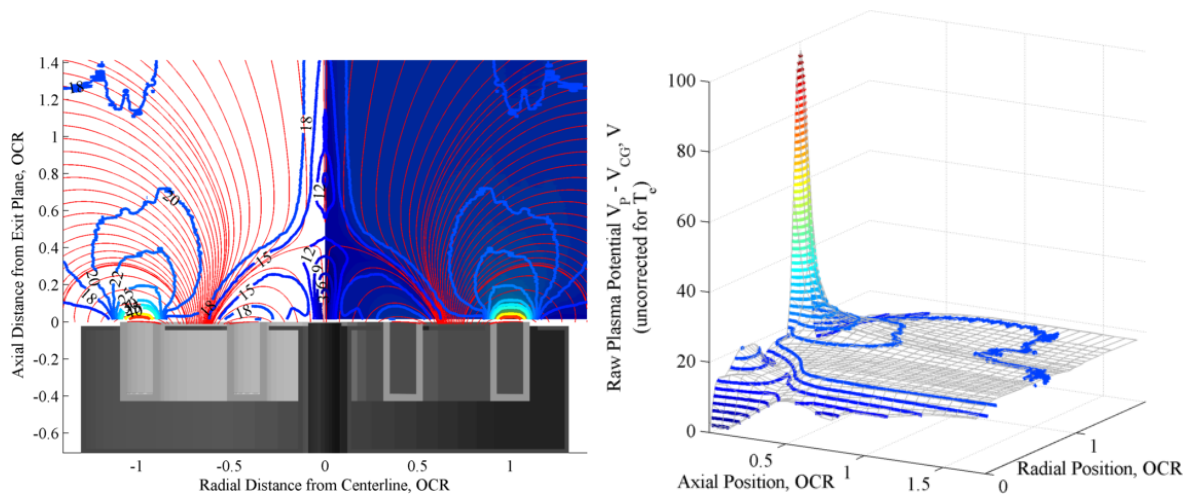


Figure 17. Raw Plasma Potential Measured from Emissive Probe, Uncorrected for T_e , Outer Channel Operation

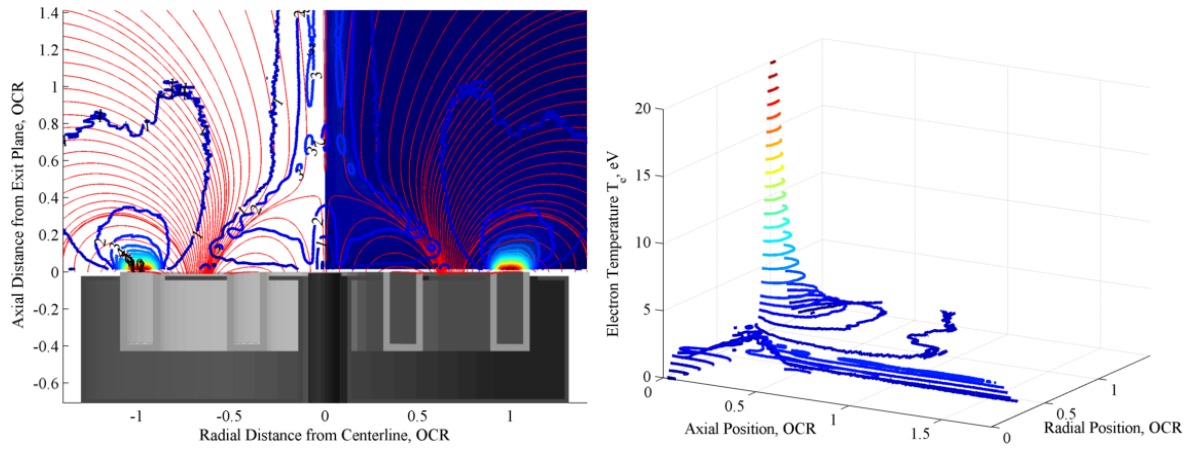


Figure 18. Estimated Electron Temperature T_e from Hot and Cold Emissive Probe Maps, Outer Channel Operation

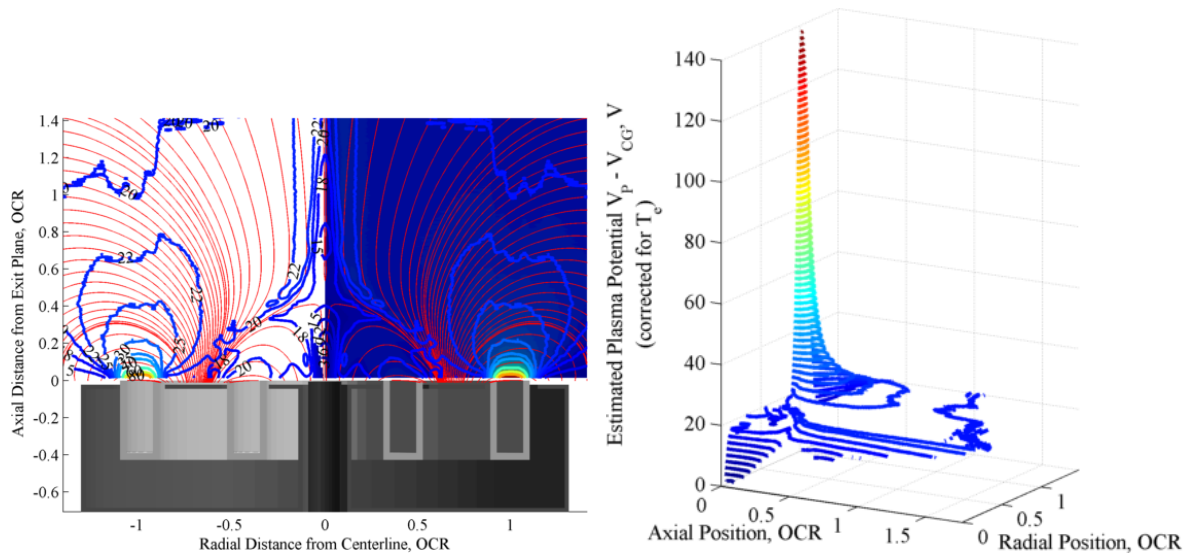


Figure 19. Estimated Plasma Potential Corrected for T_e , Outer Channel Operation

3. Dual Channel

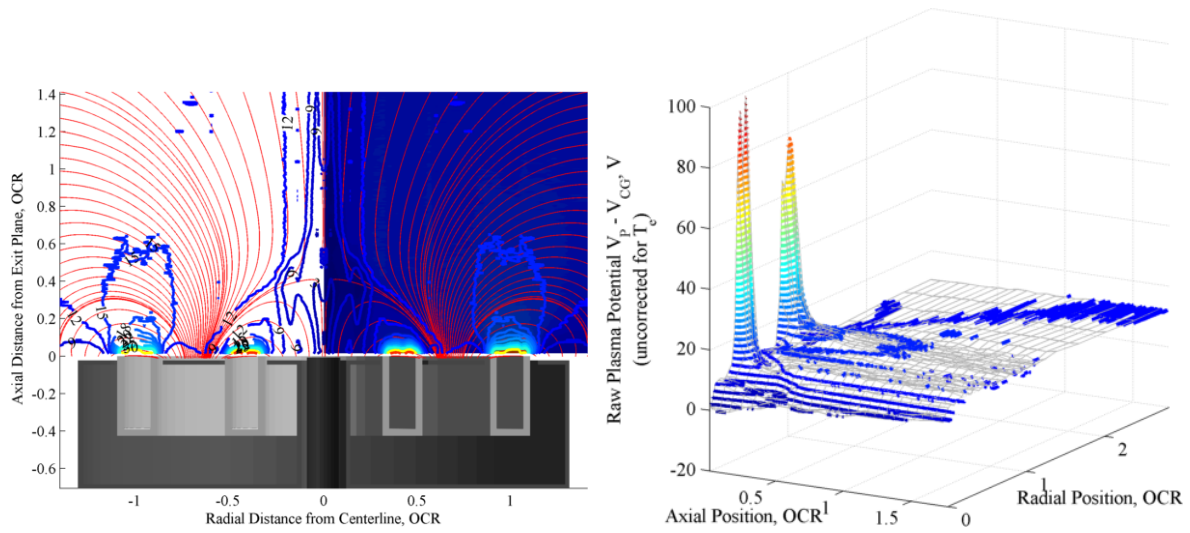


Figure 20. Raw Plasma Potential Measured from Emissive Probe, Uncorrected for T_e , Dual Channel Operation

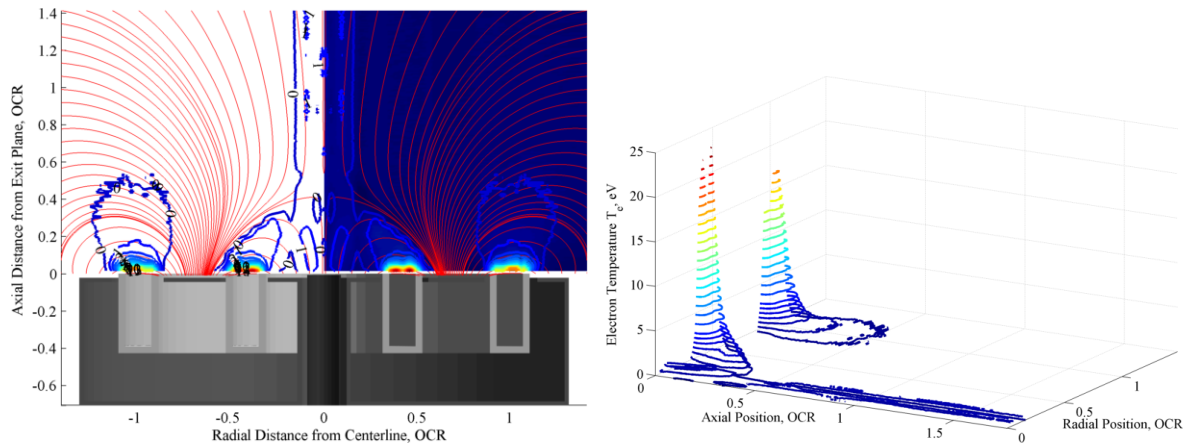


Figure 21. Estimated Electron Temperature T_e from Hot and Cold Emissive Probe Maps, Dual Channel Operation

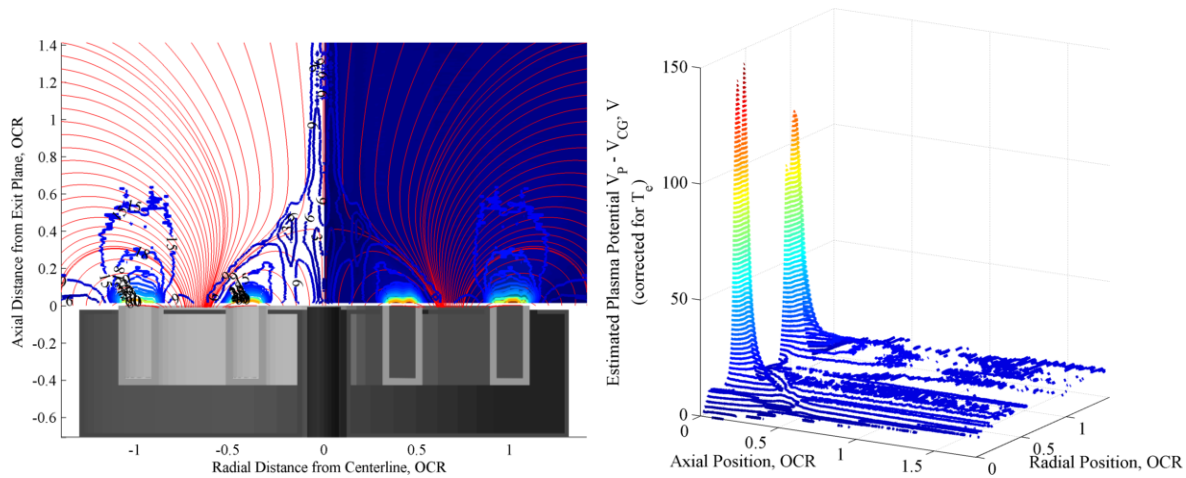


Figure 22. Estimated Plasma Potential Corrected for T_e , Dual Channel Operation

C. Fluctuation Magnitudes

This section shows fluctuation magnitudes of the plasma potential over the range of the HARP injection. The raw plasma potential is broken into the average over each millimeter bin and the RMS of the oscillations within that millimeter of travel computed after subtracting off the local mean from the signal. The amplitude of oscillations can be estimated as $\sqrt{2}$ times the RMS value plotted.

Over the course of most of the axial range, the amplitude of fluctuations in the probe potential are small and the oscillation in the cathode floating potential accounts for most of the oscillation of the total raw plasma potential ($V_p - V_{CG}$). Only in the near-field, within about $z = 0.5 \cdot OCR$, does the probe fluctuation potential increase dramatically. However, by the very near field the oscillations form a substantial fraction of the mean potential, with RMS values of 10-30 V. These values may be underestimates, since they do not account for any fluctuations in electron temperature. If T_e varies in phase with V_p , the oscillation magnitudes in the very near field could be significantly larger.

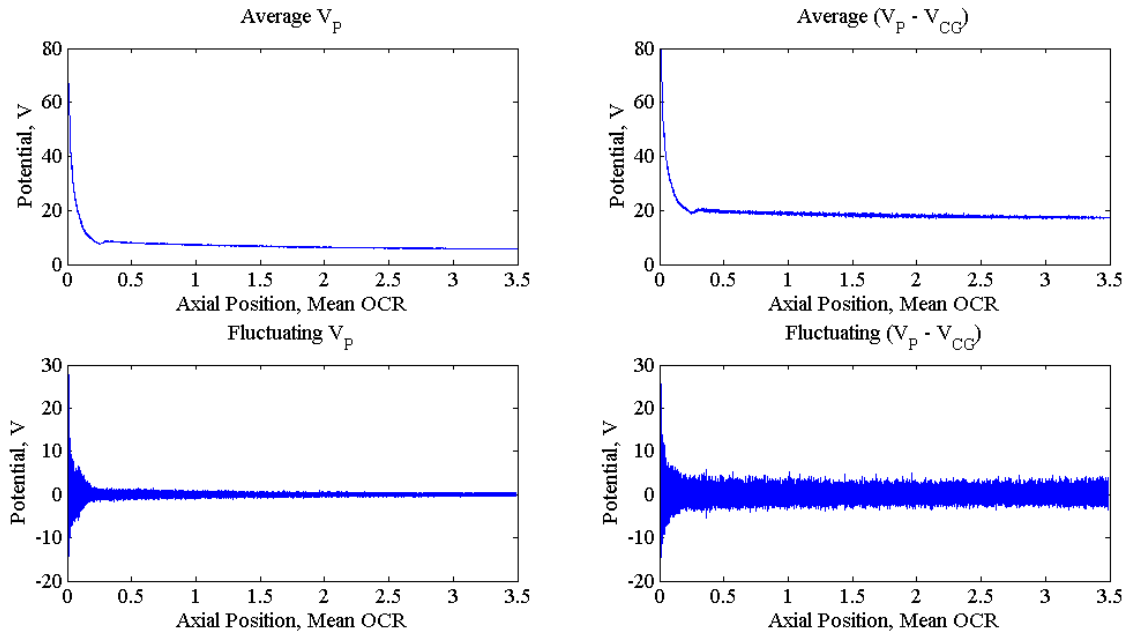


Figure 23. Mean and Fluctuating Raw Plasma Potentials, Inner Channel - Single Channel Operation

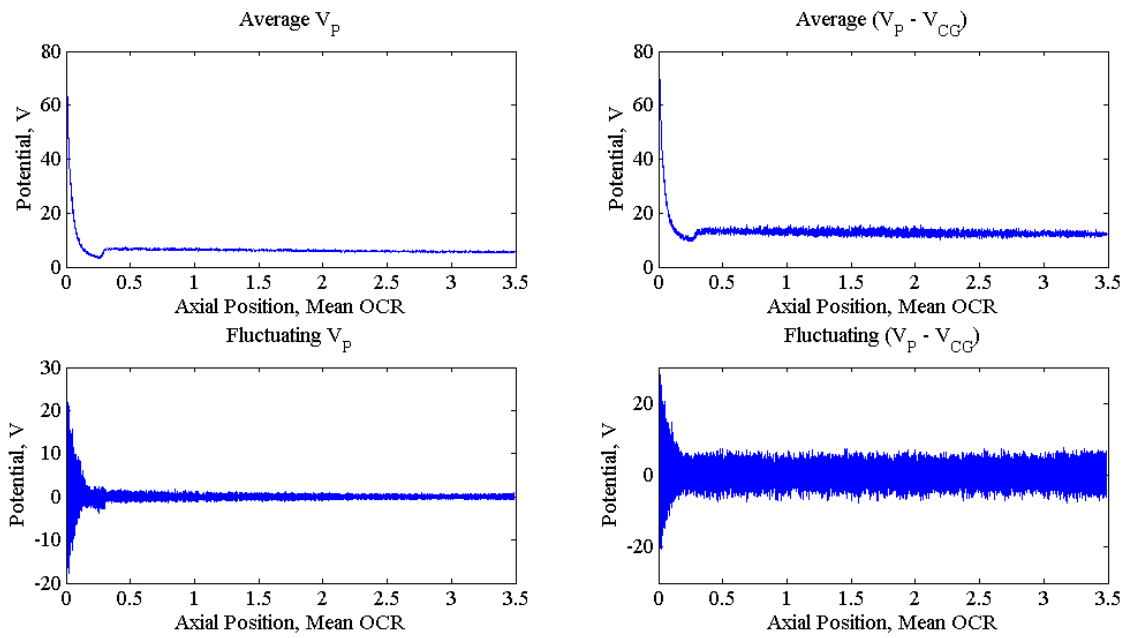


Figure 24. Mean and Fluctuating Raw Plasma Potentials, Inner Channel - Dual Channel Operation

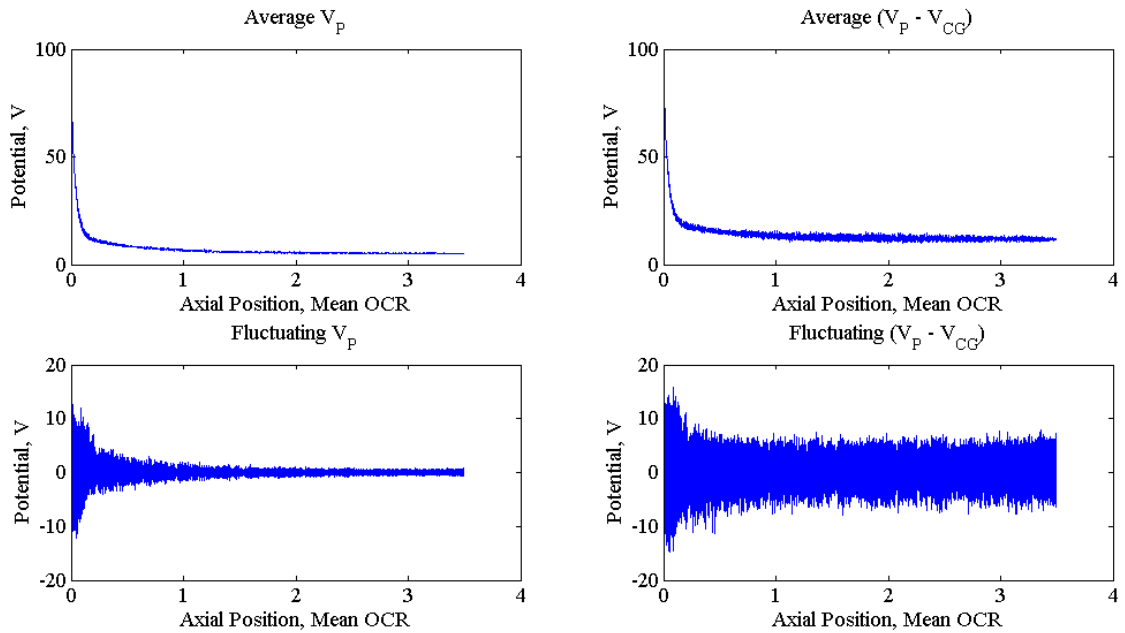


Figure 25. Mean and Fluctuating Raw Plasma Potentials, Outer Channel - Dual Channel Operation

D. Wavelet analysis of V_p

Since the cold floating potential was mapped separately from the hot plasma potential, only the uncorrected plasma potential is used for wavelet analysis. At this time wavelet analysis of probe injections over the inner and outer channel in each of single and dual channel operation is in progress, but only the injection over the outer channel during single channel operation has been completed, shown below in Figure 26.

The main takeaway from the figure is that the spoke frequencies detected in high speed imaging, shown at the top, are clearly detectable in the very near field as strong plasma potential oscillations, stronger even than the breathing mode in that region. Incredibly, several much smaller frequency modes are also apparent in the probe wavelet transform, and counting back from the clearly detected $m = 5$ and $m = 6$ modes in the video DFT, these appear to be traces of the longer wavelength, lower frequency modes $m = 1 - 4$.

VI. Key Results

Note that Figures 17 and 18 show a ripply stair-step pattern in the contours along the bell edge, an artifact of a coarse radial step size ($\sim .07$ mean OCR) for the floating potential map that causes apparent jumps when smoothed into a contour plot. Both the electron temperature and corrected plasma potential maps are less clean in this region than the raw plasma potential maps, which used a much finer radial step size.

A. Influence of Separatrix on V_p , T_e Contours

The most noticeable feature of the plasma potential and electron temperature maps are the influence of the magnetic field separatrix, visible as a bell-shaped structure in the near-field plume. Easily visible dips of several volts in plasma potential are visible in this region. Allowing for the coarse floating potential radial steps, electron temperature isotherms also follow reasonably closely along the magnetic field streamlines in the bell region. This suggests relatively easy electron transport from the cathode region out along the bell to downstream of the inner channel and potentially to the middle pole between the two channels.

B. Potential Incomplete Saturation in Dual Channel Maps

The dual channel maps suggest that, in spite of our best efforts, the probe may not have been fully saturated. The increased jitter in the data visible throughout the axial range in the contour maps and the irregular contour over the discharge channel (i.e., the double maxima in the potential near the exit plane) do not seem to have a physical basis. Nevertheless, the large plasma potentials measured by the probe suggest that, if not in full saturation, the probe was nearly saturated, and trends in the data should still be valid.

C. Detection of Spoke Plasma Potential Oscillations in Near Field

The detection of multiple spoke modes by the emissive probe is highly interesting since the wavelet analysis shows the spoke frequency oscillations to be larger in magnitude than the breathing mode frequency oscillations. Given that the total oscillation RMS values in the very near field (i.e., within the first few millimeters in front of the exit plane) are in the tens to several tens of volts, azimuthal spoke plasma potential oscillations of this order are very plausible. Since only the outer channel single channel operation data has been processed to date, future analysis will examine whether the same behavior is present over the inner channel, and whether this behavior changes going from single- to dual-channel operation.

VII. Acknowledgments

Portions of the research described in this paper were carried out at the Jet Propulsion Laboratory, California Institute of Technology, under a contract with the National Aeronautics and Space Administration. The Photron SA5 FASTCAM was made available through the support of the Michigan/AFRL Center of Excellence in Electric Propulsion (MACEEP), grant FA9550-09-1-0695, under joint program managers Dr. Mitat Birkan (AFOSR) and Dr. James Haas (AFRL/RZ). The FASTCAM video analysis in this paper would not have been possible without computing resources funded by a Strategic University Research Partnership (SURP) with the Jet Propulsion Laboratory under principal

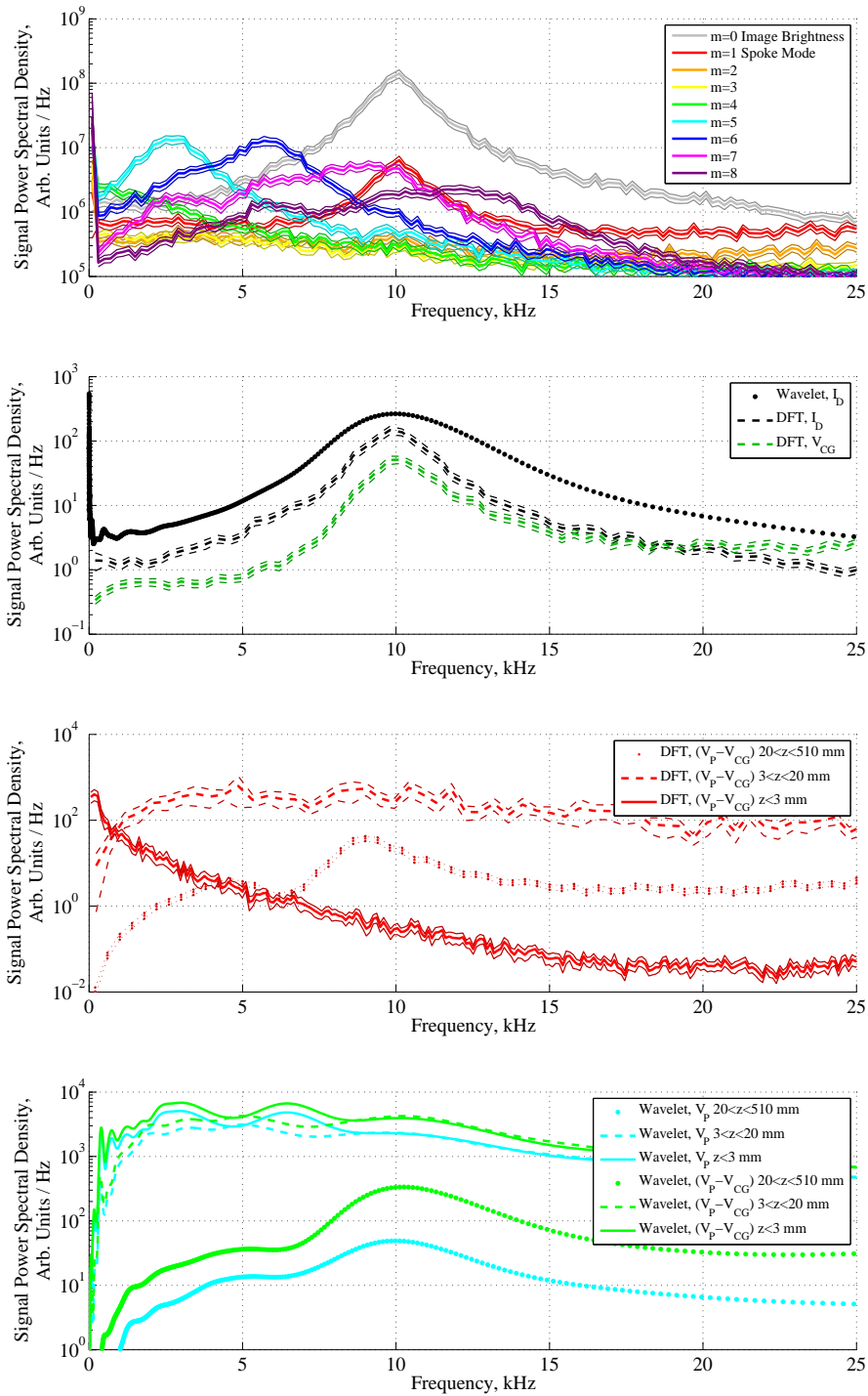


Figure 26. Collected frequency spectra for quantities of interest during emissive probe injection on X2 outer channel centerline during single channel operation. Top, FASTCAM video DFT showing spoke and breathing mode frequencies. Second from top, DFTs of discharge current and cathode floating potential confirm the breathing mode frequency, and a wavelet-generated periodogram of the discharge current demonstrates smoothing at the expense of frequency resolution. Third, DFTs of the emissive probe signal during various axial ranges illustrate the shortcomings of the DFT for turbulent signals of short duration. Bottom, wavelet-generated periodograms of the same axial ranges are far clearer, showing in particular the presence of the $m = 5$ and $m = 6$ spokes seen in the top plot, with lower frequency peaks that may be from lower spoke modes $m = 1 - 4$ not clearly detectable in the video DFT. Note that the full plasma potential ($V_P - V_{CG}$) shows a stronger signal than V_P alone.

investigator Dr. Richard Hofer. The first author is grateful for the funding support of the National Science Foundation Graduate Research Fellowship Program, the Tau Beta Pi Foundation, the National Defense Industry Association, and the aforementioned SURP. Finally, special thanks also go to PEPL doctoral candidate Ray Liang, without whose expertise, training and gracious assistance in operating the X2 (to say nothing of his design and construction of it in the first place), this work would not have been possible.

VIII. Appendix: 1D Finite Element Model for Emissive Probe Heating

This section derives a 1D finite element model for a simplified emissive probe geometry and implements it in MATLAB. The model is intended to compute the approximate heating current required to bring a filament tip to thermionic emission, and is useful for initial experiment design and sizing of power supplies. It also illustrates the sensitivity of filament temperature to small changes in heating current.

The finite element equations and boundary conditions are derived for dissimilar lead wires and filament material, with values included in the code for copper leads and a (thoriated) tungsten filament. Variation of thermal conductivity and electrical resistivity with temperature is included, though emissivity is assumed constant for each material (in reality it will vary with both temperature and surface condition).

While the model results are qualitatively correct, thermal contact resistance is not accounted for at the copper/tungsten interface. This produces a continuous profile across the interface, instead of a more realistic sharp temperature drop from the filament to the lead wire. This overestimates the copper tip temperature and underestimates the filament base temperature, though the tip temperature is still reasonably accurate for filaments with large length/diameter. As a result, the model predicts melted copper leads in many cases where experiment showed them to survive intact. In practice, even among batches of probes made as identically as possible, a spread of a few tenths of an amp in saturated heating current was observed, probably due to varied contact resistances from crimping of the copper lead wire tubes onto the tungsten filament. This only further emphasizes that this model is most useful as an initial estimate for probe heating currents – careful testing should guide the final choice of heating current.

A. Derivation of Governing Equation

To begin, consider a long, thin, resistive wire in vacuum carrying a current I . The wire will experience Ohmic heating and a combination of radiative and conductive cooling.

The power balance for a section of wire between x and $x + \Delta x$ is

$$P_c|_x - P_c|_{x+\Delta x} + P_{ohm} - P_{rad} - P_{thermionic} = 0 \quad (4)$$

where P_c is the conducted power, P_{ohm} is the Ohmic heating power, P_{rad} is the thermal radiated power and $P_{thermionic}$ is the power carried by the thermionically emitted electron current. These terms are defined as

$$P_{ohm} \equiv I^2 R = I^2 \rho \frac{\Delta x}{\pi r^2} \quad (5)$$

$$P_{rad} \equiv \sigma A_r (\epsilon_w T_w^4 - \epsilon_b T_b^4) = \sigma (2\pi r \Delta x) (\epsilon_w T_w^4 - \epsilon_b T_b^4) \quad (6)$$

$$P_{cond} \equiv kA \frac{dT}{dx} = k\pi r^2 \frac{dT}{dx} \quad (7)$$

$$P_{cond} \equiv jA_r \Phi_w = \left(A_G T_w^2 \exp\left(\frac{-q\Phi_w}{k_B T_w}\right) \right) (2\pi r \Delta x) \Phi_w \quad (8)$$

Recall by the formal definition of the derivative that

$$\frac{dP_c}{dx} \equiv \frac{P_c|_x - P_c|_{x+\Delta x}}{\Delta x} \quad (9)$$

Together, Eqns. 5, 6, 8 and 9 substitute into Eqn. 4 to yield:

$$\frac{dP_c}{dx} = -2\pi r \left(\sigma \epsilon_w T_w^4 - \sigma \epsilon_b T_b^4 + \Phi_w A_G T_w^2 \exp\left(\frac{-q\Phi_w}{k_B T_w}\right) \right) + \frac{I^2 \rho}{\pi r^2} \quad (10)$$

We can now substitute Eqn. 7 for the conducted power into Eqn. 10 and, assuming a constant thermal conductivity (i.e., $k \neq k(T)$), arrive at the governing nonlinear inhomogeneous differential equation

$$\frac{d^2 T_W}{dx^2} = aT_W^4 + bT_W^2 \exp\left(\frac{-q\Phi_W}{k_B T_W}\right) - c \quad (11)$$

where the constants a , b and c used to simplify the equation are given by

$$a \equiv \frac{2\sigma\epsilon_W}{kr} \quad (12)$$

$$b \equiv \frac{2\Phi_W A_G}{kr} \quad (13)$$

$$c \equiv \frac{2\sigma\epsilon_b T_b^4}{kr} + \frac{I^2 \rho}{k(\pi r^2)^2} \quad (14)$$

This equation is not analytically solvable, but it is amenable to iterative solution by finite elements. While k does vary with T , it will vary only slightly over each finite element so in the limit of small element size the equation will hold.

B. Discretization for Finite Element Analysis

We start by noting the finite element expressions for the first and second derivatives of an arbitrary function $y = f(x)$:

$$f'(x_i) = y'_i = \frac{y_{i+1} - y_{i-1}}{2h} - O(h^2) \quad (15)$$

$$f''(x_i) = y''_i = \frac{y_{i+1} - 2y_i + y_{i-1}}{h^2} + O(h^2) \quad (16)$$

where h is the small step size (e.g., Δx) and the primes denote derivatives. These expressions are derived from the Taylor expansion for $f(x_{i+1}) = f(x_i + h) = f(x_i) + hf'(x_i) + \dots$ as well as the expansion for $f(x_{i-1})$. Adding the two expansions and solving for $f'(x_i)$ yields Eqn. 15, while subtracting the expansions and solving for $f''(x_i)$ yields Eqn. 16. We can now substitute into Eqn. 11 and solve for

$$T_i = \frac{1}{3}(T_{i+1} + T_i + T_{i-1}) + \frac{h^2}{3} \left(-aT_i^4 - bT_W^2 \exp\left(\frac{-q\Phi_W}{k_B T_W}\right) + c \right) \quad (17)$$

This finite element expression has two pieces. The first term on the RHS is a relaxation term, tending to bring the temperature of each node to an average with its neighbors. In the absence of heating, this would be the only term and the temperature profile would be linear between any imposed boundary conditions. The second term on the RHS holds the heating and cooling terms, which complicate the profile.

C. Boundary Conditions

The finite element simulation is complete in principle when boundary conditions are applied, either by specifying T or dT/dx at each end of the filament. It is unrealistic to fix T at the filament-lead wire joint since this temperature varies strongly with filament length and both filament and lead wire diameter and material. It is more reasonable to assume that the distant ends of the filament lead wires are close to room temperature, at the cost of introducing the filament-lead wire interface into the simulation domain. This requires a further interface boundary condition depending on the material properties that we now derive.

We consider the copper tube / tungsten wire connection in a linear geometry and planar material interface that simplifies the model while retaining the essential features (Figure 7). For generality we label the copper as material 1 and the tungsten as material 2, and permit different finite element sizes h_1 and h_2 in each material. Physically, the interface temperature T_x will not just be an average of the node temperatures T_1 and T_2 to either side. The copper is more conductive and has a larger cross section than the filament, so T_x should be closer to T_1 than T_2 if $h_1 \approx h_2$.



Figure 27. The hairpin filament geometry is simplified to a purely linear geometry with a planar material interface in the 1D finite element model.

By conservation of energy, the heat conducted from the filament is equal to the heat conducted into the copper:

$$-k_1 A_1 \left. \frac{dT}{dx} \right|_1 = -k_2 A_2 \left. \frac{dT}{dx} \right|_2 \quad (18)$$

We can also write T_x in terms of either T_1 or T_2 :

$$T_x = T_1 + dT_1 = T_1 + h_1 \left. \frac{dT}{dx} \right|_1 \quad (19)$$

$$T_x = T_2 - dT_2 = T_2 - h_2 \left. \frac{dT}{dx} \right|_2 \quad (20)$$

Equating Eqns. 19 and 20,

$$T_1 + h_1 \left. \frac{dT}{dx} \right|_1 = T_2 - h_2 \left. \frac{dT}{dx} \right|_2 \quad (21)$$

Substituting in from Eqn. 18 yields

$$T_1 + h_1 \left. \frac{dT}{dx} \right|_1 = T_2 - h_2 \frac{k_1 A_1}{k_2 A_2} \left. \frac{dT}{dx} \right|_1 \quad (22)$$

Solving for the derivative and substituting back into Eqn. (16) then gives an expression for T_x in terms of only the temperatures T_1 and T_2 and the known step sizes and material properties h , k and A :

$$T_x = T_1 \left(1 + \frac{\frac{T_2}{T_1} - 1}{\frac{h_2 k_1 A_1}{h_1 k_2 A_2} + 1} \right) \quad (23)$$

As a reality check, in the limit as $h_2/h_1 \rightarrow 0$, $T_x \rightarrow T_2$. As $h_2/h_1 \rightarrow \infty$, $T_x \rightarrow T_1$.

D. Material Properties

Electrical resistivity ρ , thermal conductivity k , and radiative emissivity ϵ all vary with temperature for real materials. These effects have been included for ρ and k in the model, with values for pure tungsten used for the thoriated tungsten filament. The emissivities are assumed constant with a value of 0.5 for tungsten and 0.05 for copper. The model is sensitive to emissivity and conductivity, so better accounting for the emissivity would improve model fidelity, but since the emissivity also depends on surface condition it is difficult to account for well.

Recommended thermal conductivities as a function of temperature are obtained from Ho and Powell², and quadratic fits to the empirical data are applied in the temperature region of interest in Figure 28. Tungsten resistivity values are fit from data by Savitskii, while copper resistivity is obtained from the CRC handbook.^{27?}

E. Code Implementation

The finite element governing equation, Eqn. (14), the interface boundary condition Eqn. (20) and the endpoint boundary conditions setting the distant lead wire ends to room temperature are implemented in MATLAB at the end of the Appendix. An initial flat temperature profile seeds the code which then computes new T_i 's from the old on each iteration. Once a temperature convergence criterion is satisfied on a coarse mesh, the coarse solution is interpolated to

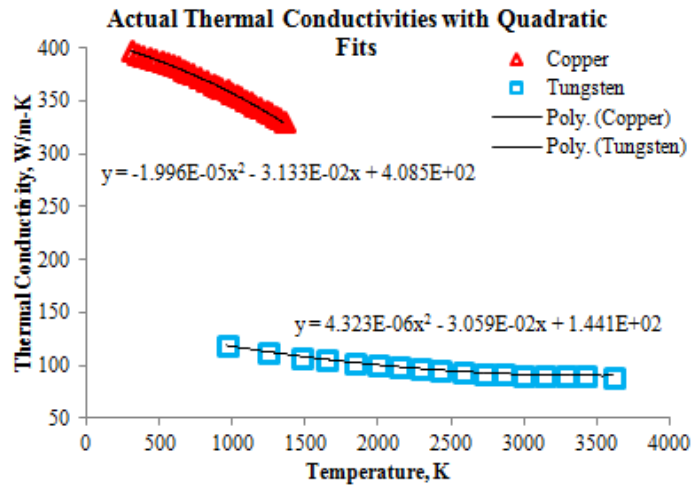


Figure 28. Thermal conductivities

a finer resolution and recomputed until successively finer mesh solutions differ by no more than a second convergence criterion. By default these criteria are set at 10^{-6} K and 10 K, respectively.

The simulation is also sensitive to the lead wire material, diameter, and length. Beyond a certain point it is not sensitive to filament length, as the wire approaches the long-wire limit and conduction becomes weak compared to radiation and electron emission.

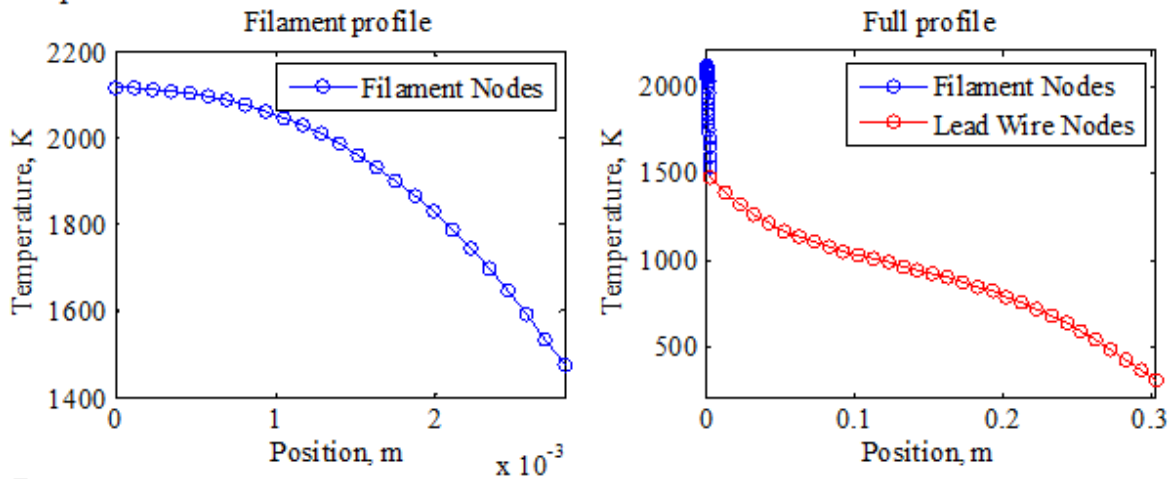


Figure 29. Example code output, showing temperature profile in filament and lead wires

E. Code

```

function [maxT_w,maxT_cu] = EmissiveProbeThermalModel()
%% [maxT_w,maxT_cu] = EmissiveProbeThermalModel()
% This function solves coupled radiation and conduction equations to
% compute the thermal profile of a resistively heated tungsten wire with
% lead wires of dissimilar material. Details are discussed in the text.
% All units are SI base units (meters, amperes, Kelvin, etc.)
tic; clc; close all
if nargin==0 % Set default values here or run from command line
    maxsteps = 1e4; % max iterations (user discretion)
    Lcu = 0.300; % copper lead wire length, meters
    Lw = 0.0056; % filament length, meters
    maxerr = 1e-6; % convergence limit (K) when iterating
    I = 2.2; % filament heating current, amperes
    T0 = 300; % lead wire endpoint boundary condition
    TempThreshold = 10; % convergence limit (K) when doubling filament nodes
end

%% ----- Constants -----
% Fundamental constants
sigma = 5.670373e-8; % stefan boltzmann constant, W/m^2-K
k_b = 1.38e-23; % boltzmann constant, J/K
q = 1.602e-19; % electron charge
% Material properties (L_w = Tungsten, L_cu = Copper)
eps_cu = 0.05; eps_w = 0.5; % emissivity, unitless
rho_cu0 = 1.678e-8; rho_w0 = 5.28e-8; % resistivity, ohm-meters
alpha_cu = 3.9e-3; alpha_w = 5.522e-3; % temp. coeff. of resist., 1/K
rho_w = @(T) rho_w0 * (1 + alpha_w*(T-293)); % W resistivity as f(T)
rho_cu = @(T) rho_cu0 * (1 + alpha_cu*(T-293)); % Cu resistivity as f(T)
k_cu = 400; k_w = 100; % thermal conductivity, W/m-K
phi_w_th = 2.6; % W/Th work function, volts
Ag_w_th = 3e4; % W/Th Richardson-Dushman A_G

% Background emissivity and temperature
eps_b = 1; Tb = 300;
% Filament properties (meters)
D = .004*25.4/1e3; r_w = D/2; A_w = pi*r_w^2;
% Copper tube lead wire properties (meters)
OD_cu = .4064e-3; ID_cu = .1270e-3; % outer, inner diameters
A_cu = pi/4*(OD_cu^2-ID_cu^2); r_cu_eff = sqrt(A_cu/pi);

% Constant factors, computed outside loop for speed
a1_cu = 2*sigma*eps_cu/r_cu_eff; a1_w = 2*sigma*eps_w/r_w;
b1_w = 2*phi_w_th*Ag_w_th/r_w;
c1_cu = 2*sigma*eps_b*Tb^4/r_cu_eff; c1_w = 2*sigma*eps_b*Tb^4/r_w;
c2_cu = I^2/(A_cu^2); c2_w = I^2/(A_w^2);

%% ----- Finite element setup -----
% Number of nodes, node intervals, and coordinates (only 1/2 W simulated)
Nw = max(ceil(Lw/.001),2); Ncu = max(Lcu/.01,10);
h_w = 0.5 * Lw/Nw; h_cu = Lcu/Ncu;
x_w = linspace(0,Lw/2,Nw+1); x_cu = linspace(Lw/2,Lw/2+Lcu,Ncu+1);

% Guess a constant flat temperature profile to seed the iteration
T_cu = T0*ones(1,Ncu+1); T_w = T0*ones(1,Nw+1);

%% ----- Main loop -----
FiniteError = TempThreshold+1;
while FiniteError>TempThreshold
    T = [T_w T_cu]; i = 0; err = maxerr+1; Tnew = 0;
    while i<maxsteps && max(err)>maxerr
        % Compute relaxation terms (Length N-1; endpoints found separately)
        relax_cu = 1/3 * (T_cu(1:Ncu-1) + T_cu(2:Ncu) + T_cu(3:Ncu+1));
        relax_w = 1/3 * (T_w(1:Nw-1) + T_w(2:Nw) + T_w(3:Nw+1));

        % Compute node temperatures w/ relaxation + heating/cooling terms
        Tnew_cu = relax_cu + h_cu^2/(3*k_cu).*(-a1_cu*T_cu(2:Ncu).^4 ...
            + c1_cu + c2_cu*rho_cu(T_cu(2:Ncu)));
        Tnew_w = relax_w + h_w^2/(3*k_w).*(-a1_w*T_w(2:Nw).^4 ...
            -b1_w*T_w(2:Nw).^2.*exp(-q*phi_w_th./(k_b*T_w(2:Nw))) ...
            + c1_w + c2_w*rho_w(T_w(2:Nw)));

        % Apply interface boundary condition for T_cu(end) = T_w(1)
        x1 = (h_cu/h_w) * (k_w*A_w)/(k_cu*A_cu);
        dT1 = (Tnew_cu(1) - Tnew_w(end)) / (x1+1);
        T_w(end) = Tnew_w(end) + dT1; T_cu(1) = T_w(end);

        % Compute new filament midpoint temp
        T_w(1) = 1/3*(2*Tnew_w(1)+T_w(1)) + h_w^2/(3*k_w) ...
            *( -a1_w*T_w(1).^4 -b1_w*T_w(1).^2.*exp(-q*phi_w_th/(k_b*T_w(1))) ...
            + c1_w + c2_w*rho_w(T_w(1)));

        % Save newly computed temps and compute error from last iteration
        T_cu(2:Ncu) = Tnew_cu; T_w(2:Nw) = Tnew_w;
        err = max(abs([T_w T_cu]-Tnew));
        Tnew = [T_w T_cu]; i=i+1;
    end

    FiniteError = max(abs(T-Tnew));
    if FiniteError>TempThreshold
        % Double number of filament nodes and halve spacing
        Nw = Nw*2; h_w = 0.5 * Lw/Nw;
        % Interpolate temperatures from old coarse nodes to new finer nodes
        xi_w = linspace(0,x_cu(1),Nw+1);
        T_w = interp1(x_w,T_w,xi_w,'pchip'); x_w = xi_w;
    end
end

%% ----- Report results and plot -----
maxT_w = max(T_w); maxT_cu = max(T_cu);
fprintf('Max filament temp: %4.0f K\rMax copper temp: %4.0f K\r', [maxT_w maxT_cu])
if i>maxsteps;
disp(['Insufficient convergence / max iterations exceeded. Adjust ''maxsteps'' or ''maxerr''.']);
end
if nargin==0
    subplot(1,2,1); plot([x_w,[T_w]'],'-o'); xlim([0,Lw/2])
    xlabel('Position, m'); ylabel('Temperature, K'); title('Filament profile')
    legend('Filament Nodes')
    subplot(1,2,2); plot(x_w,T_w,'b-o',x_cu,T_cu,'r-o'); xlim([0,Lcu+Lw/2])
    xlabel('Position, m'); ylabel('Temperature, K'); title('Full profile')
    legend('Filament Nodes','Lead Wire Nodes'); clear all; toc
end

```

References

- ¹McDonald, M. S., Sekerak, M. J., Gallimore, A. D., and Hofer, R. R., "Plasma Oscillation Effects on Nested Hall Thruster Operation and Stability," *2010 IEEE Aerospace Conference*, IEEEAC Paper #2502, Big Sky, MT, March 2013, pp. 1–9.
- ²Liang, R., *The Combination of Two Concentric Discharge Channels into a Nested Hall-Effect Thruster*, Ph.D. thesis, University of Michigan, Ann Arbor, MI, 2012.
- ³Liang, R. and Gallimore, A. D., "Constant-Power Performance and Plume Measurements of a Nested-Channel Hall-Effect Thruster," *32nd International Electric Propulsion Conference*, IEPC 2011-049, Wiesbaden, Germany, 2011.
- ⁴Jacobson, D. T., John, J. W., Kamhawi, H., Manzella, D. H., and Peterson, P. Y., "An Overview of Hall Thruster Development at NASA's John H. Glenn Research Center," *41st AIAA/ASME/SAE/ASEE Joint Propulsion Conference & Exhibit*, AIAA 2005-4242, Tucson, AZ, July 2005.
- ⁵Spores, R., Monheiser, J., Dempsey, B. P., Wade, D., Creel, K., Jacobson, D., and Drummond, J., "A Solar Electric Propulsion Cargo Vehicle to Support NASA Lunar Exploration Program," Princeton, New Jersey (USA), 2005, pp. IEPC-2005-320.
- ⁶Liang, R. and Gallimore, A., "Far-Field Plume Measurements of a Nested-Channel Hall-Effect Thruster," *49th AIAA Aerospace Sciences Meeting*, AIAA-2011-1016, Jan. 2011.
- ⁷Goebel, D. M. and Watkins, R. M., "Compact lanthanum hexaboride hollow cathode," *Review of Scientific Instruments*, Vol. 81, No. 8, 2010, pp. 083504.
- ⁸Hofer, R. R., *Development and Characterization of High-Efficiency, High-Specific Impulse Xenon Hall Thrusters*, Ph.D. thesis, University of Michigan, 2004.
- ⁹Brown, D., Larson, C., Beal, B., and Gallimore, A., "Methodology and Historical Perspective of a Hall Thruster Efficiency Analysis," *Journal of Propulsion and Power*, Vol. 25, No. 6, 2009, pp. 1163–1177.
- ¹⁰Sheehan, J. P., Raitses, Y., Hershkowitz, N., Kaganovich, I. D., and Fisch, N. J., "The use of electric probe techniques for electric potential measurements in plasma thrusters," *32nd International Electric Propulsion Conference*, IEPC 2011-174, Wiesbaden, Germany, 2011.
- ¹¹Haas, J. M., Gallimore, A. D., McFall, K., and Spanjers, G., "Development of a high-speed, reciprocating electrostatic probe system for Hall thruster interrogation," *Review of Scientific Instruments*, Vol. 71, No. 11, Nov. 2000, pp. 4131–4138.
- ¹²McDonald, M. and Gallimore, A., "2013 IEPC Spoke Paper," *33rd International Electric Propulsion Conference*, IEPC 2013-XXX, Washington, DC, USA, 2013.
- ¹³McDonald, M. and Gallimore, A., "Parametric Investigation of the Rotating Spoke Instability in Hall Thrusters," *32nd International Electric Propulsion Conference*, IEPC 2011-242, Wiesbaden, Germany, 2011.
- ¹⁴McDonald, M. S., *Electron Transport in Hall Thrusters*, Ph.D. thesis, University of Michigan, Ann Arbor, MI, 2011.
- ¹⁵McDonald, M. S. and Gallimore, A. D., "Measurement of Cross-Field Electron Current in a Hall Thruster Due to Rotating Spoke Instabilities," *47th AIAA/ASME/SAE/ASEE Joint Propulsion Conference & Exhibit*, AIAA 2011-5810, 2011.
- ¹⁶Haas, J. M. and Gallimore, A. D., "Internal plasma potential profiles in a laboratory-model Hall thruster," *Physics of Plasmas*, Vol. 8, No. 2, 2001, pp. 652.
- ¹⁷Linnell, J. A. and Gallimore, A. D., "Internal plasma potential measurements of a Hall thruster using plasma lens focusing," *Physics of Plasmas*, Vol. 13, No. 10, Oct. 2006, pp. 103504–103504-9.
- ¹⁸Linnell, J. A. and Gallimore, A. D., "Internal plasma potential measurements of a Hall thruster using xenon and krypton propellant," *Physics of Plasmas*, Vol. 13, No. 9, Sept. 2006, pp. 093502–093502-10.
- ¹⁹Jameson, K., *Investigation of Hollow Cathode Effects on Total Thruster Efficiency in a 6-kW Hall Thruster*, Ph.D. thesis, University of California Los Angeles, Los Angeles, CA, 2008.
- ²⁰Reid, B. M. and Gallimore, A. D., "Plasma Potential Measurements in the Discharge Channel of a 6-kW Hall Thruster," *44th AIAA/ASME/SAE/ASEE Joint Propulsion Conference & Exhibit*, AIAA 2008-5185, 2008.
- ²¹Hargus, W. A., *Investigation of the Plasma Acceleration Mechanism within a Coaxial Hall Thruster*, Ph.D. thesis, Stanford University, Palo Alto, CA, 2001.
- ²²Jameson, K., Goebel, D., Hofer, R., and Watkins, R., "Cathode Coupling in Hall Thrusters," Florence, Italy, Sept. 2007, pp. IEPC 2007-278.
- ²³Langmuir, I., "The Electron Emission from Thoriated Tungsten Filaments," *Physical Review*, Vol. 22, No. 4, Oct. 1923, pp. 357–398.
- ²⁴Harbaugh, W. E., "Tungsten, Thoriated-Tungsten, and Thoria Emitters," *Electron Tube Design*, Radio Corporation of America, Electron Tube Division, Harrison, New Jersey, 1st ed., 1962, pp. 90–98.
- ²⁵Lassner, E. and Schubert, W.-D., *Tungsten: Properties, Chemistry, Technology of the Element, Alloys, and Chemical Compounds*, Springer, 1999.
- ²⁶Crowell, C., "The Richardson constant for thermionic emission in Schottky barrier diodes," *Solid-State Electronics*, Vol. 8, No. 4, April 1965, pp. 395–399.
- ²⁷*CRC Handbook of Chemistry and Physics*, CRC Press, Boca Raton, FL, 92nd ed., 2012.
- ²⁸Langmuir, I., "The Electron Emission from Tungsten Filaments, containing Thorium," *Physical Review*, Vol. 4, No. 6, Dec. 1914, pp. 544–545.
- ²⁹Kemp, R. F. and Sellen, J. M., "Plasma Potential Measurements by Electron Emissive Probes," *Review of Scientific Instruments*, Vol. 37, No. 4, April 1966, pp. 455–461.
- ³⁰Dannenmayer, K., Kudrna, P., Tichý, M., and Mazouffre, S., "Measurement of plasma parameters in the far-field plume of a Hall effect thruster," *Plasma Sources Science and Technology*, Vol. 20, No. 6, Dec. 2011, pp. 065012.
- ³¹McAabel, W. E., *Probe measurements*, Tektronix, 2nd ed., 1971.
- ³²Hiscocks, P. D. and Gaston, J., "Oscilloscope Probes: Theory and Practice," *Application Note*, Vol. Syscomp Electronic Design, Ltd., July 2007.
- ³³Edwards, D., "Uncarburized thoriated tungsten filament activation," *Journal of Vacuum Science and Technology*, Vol. 15, No. 1, Jan. 1978, pp. 128.
- ³⁴Lobbia, R. B. and Gallimore, A. D., "High-speed dual Langmuir probe," *Review of Scientific Instruments*, Vol. 81, No. 7, 2010, pp. 073503.

³⁵Torrence, C. and Compo, G. P., "A Practical Guide to Wavelet Analysis," *Bulletin of the American Meteorological Society*, Vol. 79, No. 1, Jan. 1998, pp. 61–78.

³⁶Raitses, Y., Staack, D., Smirnov, A., and Fisch, N. J., "Space charge saturated sheath regime and electron temperature saturation in Hall thrusters," *Physics of Plasmas*, Vol. 12, No. 7, July 2005, pp. 073507–073507–10.